Geochemistry, Geophysics, Geosystems

RESEARCH ARTICLE
10.1029/2018GC008132

Special Section:
Magnetism in the Geosciences - Advances and Perspectives

Magnetic Mineralogy and Petrophysical Properties of Ultramafic Rocks: Consequences for Crustal Magnetism

Geertje W. ter Maat[1], Suzanne A. McEnroe[1], Nathan S. Church[1], and Rune B. Larsen[1]

[1]Department of Geoscience and Petroleum, Norwegian University of Science and Technology, Trondheim, Norway

Abstract Magnetic properties from the Reinfjord Ultramafic Complex, in northern Norway, which formed as part of a deep magmatic conduit system, have been investigated to determine the magnetic signature of ultramafic rocks now exposed at the surface and deeper in the lower crust. The dominant carriers in these ultramafic rocks are a chrome-spinel with Fe-rich exsolution blebs and exsolution lamellae of magnetite in clinopyroxene. Except locally, in a fault zone and in discrete small fractures, these rocks show only minor to no alteration. We infer that the magnetic oxides characterized here are representative of pristine magnetic carriers in similar rocks deeper in the crust. These oxides can be stable in lower crustal, possibly upper mantle, depths when temperatures are below the Curie temperature of magnetite, taking into account pressure effects. These ultramafic rocks are candidates for potential sources of long-wavelength anomalies.

Plain Language Summary Satellites are used to map the Earth's magnetic field and explore magnetic anomalies created by this field in crustal rocks. To understand the magnetic signal from deep-seated rocks, we need to explore the sources and nature of the magnetic mineralogy. This paper reviews the magnetic properties of rocks that formed deep in the Earth's crust (at 25- to 35-km depth), 570–560 million years ago, now well exposed in Northern Norway. Despite a history of being exhumed from deep in the crust, these rocks only show minimal alteration and present a rare opportunity to study their pristine magnetic properties. The primary magnetic minerals in these ultramafic rocks are an exsolved chrome-spinel, and magnetite lamellae in clinopyroxene. These minerals formed at high temperatures and could be representative of minerals residing deeper in the lower or upper mantle. These phases are magnetically stable up to the Curie temperature of magnetite. These ultramafic rocks are a potential source of magnetization in the lower crust and the upper mantle.

Key Points:
- Primary magnetic oxides are chrome-spinel with Fe-rich exsolution lamellae and magnetite lamellae in pyroxene
- These carriers are stable at lower crust to uppermost mantle conditions
- Ultramafic rocks are potential sources of long-wavelength-anomalies

Supporting Information:
- Supporting Information S1
- Table S1
- Figure S1

Correspondence to:
G. W. ter Maat,
geertjetermaat@gmail.com

Citation:
ter Maat, G. W., McEnroe, S. A., Church, N. S., & Larsen, R. B. (2019). Magnetic mineralogy and petrophysical properties of ultramafic rocks: Consequences for crustal magnetism. *Geochemistry, Geophysics, Geosystems*, *20*, 1794–1817. https://doi.org/10.1029/2018GC008132

Received 6 DEC 2018
Accepted 5 FEB 2019
Accepted article online 8 MAR 2019
Published online 8 APR 2019

1. Introduction

Magnetic anomalies, at all length scales, provide evidence about subsurface features and the magnetic properties of buried rock bodies. Magnetic surveys are a powerful tool to locate and map natural resources, to study tectonic processes and geodynamic settings, and to infer the structure of the magnetic lithosphere. Suggestive, though inconclusive evidence on the lithospheric structure is given by the long-wavelength anomalies (LWAs; 500–2,500 km Ravat et al., 2002) mapped by the current SWARM and older satellite surveys. LWAs conceivably could be accounted for by regional-scale structures at shallow-to-intermediate depths, or by smaller, deeper magnetic sources. Shallower features, which could explain observed LWAs, have not been identified. The search for deeper sources has been a subject of study over the past four decades (Purucker & Whaler, 2015). A number of questions remain unresolved concerning the source of deep magnetization that could account for LWAs: Are there primary magnetic minerals in the deep lithosphere? How strongly magnetic are these minerals under deep crustal conditions? What are the effects of pressure and temperature (P&T) on the stability of the magnetic phases?

The limiting depth of magnetic sources is the Curie isotherm (e.g., 580 °C for magnetite). Earlier studies examining sources of LWAs in the mantle (Wasilewski & Mayhew, 1992; Wasilewski et al., 1979) argue that the Curie depth coincides with the continental Moho. They report the dominant magnetic mineralogy in continental mantle xenoliths to be (Cr, Mg, Al, and Fe)-spinel and conclude such compositions to be above their Curie temperature at mantle depths. Furthermore, models by Wasilewski and Mayhew (1982) calculate that deep sources of LWAs require a magnetization of 2–6 A/m. Studies of deep crustal mafic granulites

where magnetite is the dominant magnetic carrier (Warner & Wasilewski, 1995; Wasilewski & Mayhew, 1982; Wasilewski & Mayhew, 1992; Wasilewski & Warner, 1988; Williams et al., 1985) conclude that the measured room-temperature magnetizations do not attain this value and hence are certainly too weak to be a source of LWAs at mantle depths (Mayhew et al., 1991; Wasilewski & Mayhew, 1982). At depth the remanent component of the total magnetization would be lower than at surface conditions, while the induced magnetization could increase due to an enhancement of susceptibility approaching the Hopkinson peak (Dunlop et al., 2010; Kiss et al., 2005).

More recent studies claim that the upper mantle can be magnetic (e.g., Ferré et al., 2013, 2014) and that the Moho is not the magnetic boundary. Spectral analysis over cratons suggests that sources at mantle depths can contribute to anomalies where the heat flow is low (Idárraga-García & Vargas, 2018). A number of possible geodynamic settings and deep-Earth processes have been proposed to explain potential magnetic sources at depth. Studies of mantle xenoliths (Ferré et al., 2013, 2014; Friedman et al., 2014; Li et al., 2014; Liu et al., 2013; Martín-Hernández et al., 2014) provide data on the magnetization of upper-mantle rocks, which could contribute to LWAs when in situ. An alternative deep crustal or upper mantle source of magnetic anomalies deep are ultramafic rocks in suture zones containing metamorphosed serpentinites (Shive et al., 1988) or where serpentinite is actively subducted (Blakely et al., 2005).

An essential problem in attributing LWA observations to sources deep in the crust is identifying the magnetic carrier. Magnetite is usually considered the predominant magnetic mineral in the deep crust (e.g., Frost & Shive, 1986; Pilkington & Percival, 1999; Schlinger, 1985). However, the hematite-ilmenite solid solution should also be considered as stable sources of remanent magnetization (Robinson et al., 2016) and as a source for short- and long-wavelength anomalies (Brown & McEnroe, 2008; Kasama et al., 2004; Kletetschka & Stout, 1998; McEnroe & Brown, 2000; McEnroe et al., 2001a, 2001b, 2009, 2002, 2004, 2007, 2016, 2018). The high stability and unblocking temperatures of exsolved phases in the hematite-ilmenite system increase the remanent contribution to the total magnetization (McCammon et al., 2009; McEnroe & Brown, 2000; McEnroe et al., 2001a, 2001c, 2002, 2004, 2007, 2018). Chrome-spinel can also be stable at lower-crustal and upper-mantle levels (Barnes & Roeder, 2001; Wasilewski & Mayhew, 1992; Wasilewski et al., 1979); however, whether this phase is magnetic is controlled by the composition (Francombe, 1957; Ziemniak & Castelli, 2003).

Commonly, samples from exhumed deep-crustal rocks show evidence of a later lower P&T metamorphic overprint due to retrograde metamorphism (Strada et al., 2006). Identifying the magnetic phases that are stable at high P&T is challenging because many show disequilibrium microtextures that developed during the exhumation process (McEnroe et al., 2018). Equally challenging is obtaining a large suite of pristine deep-crustal samples due to the ease with which these (commonly ultramafic) rocks alter in the presence of fluid. Serpentinization of mafic minerals (e.g., olivine and pyroxene) typically at low temperatures (200–400 °C) results in the production of magnetite and a decrease in density. In many of the studies that report magnetization values from deep crustal or mantle sources, the carrier is commonly secondary magnetite derived from serpentinization. Subduction of serpentinized forearc mantle (Blakely et al., 2005; Bostock et al., 2002; Hyndman & Peacock, 2003) or in situ serpentinization of the mantle (Facer et al., 2009) have been proposed as processes that result in the presence of secondary magnetite at depth. The formation of magnetite is partially dependent of the original bulk composition of the serpentinized rocks (Bach et al., 2006; Klein et al., 2014, 2009). The amount of magnetite formed is not linearly related to the degree of serpentinization and is considered to peak at >60–70% serpentinization (Bach et al., 2006; Oufi, 2002).

Here, we examine the magnetic properties of the Reinfjord Ultramafic Complex (RUC), a deep-seated igneous conduit system in northern Norway, which is part of the Seiland Igneous Province (SIP; Figure 1). The RUC is one of four major ultramafic intrusive conduit feeders for the formation of the SIP (Grant et al., 2016; Larsen et al., 2018) and consists of at least 6.5 km^3 of ultramafic rocks (Pastore, 2018). Exposures of deep-crustal ultramafic conduits systems are relatively rare. Similar ultramafic complexes include the Chilas complex, Pakistan (Jagoutz et al., 2006; Jagoutz et al., 2007), the Abulangdang intrusion in the Emeishan large igneous province, China (Wang et al., 2014), and Kondyor, Russia (Burg et al., 2009), though late-stage alteration is common in these intrusions. The RUC is unusual in having superb exposure (Figure 2) and only local or minor alteration to the ultramafic units (Grant et al., 2016).

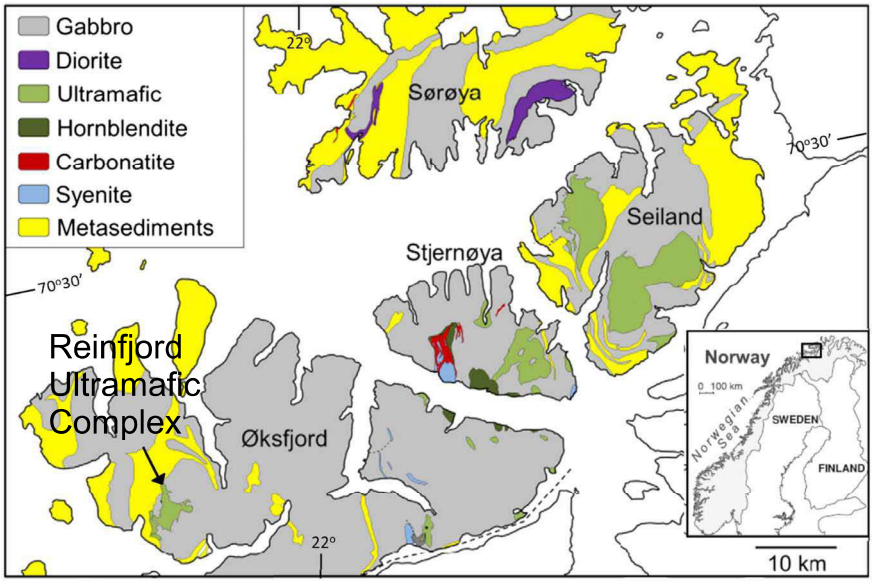

Figure 1. Map of the Seiland Igneous Province in northern Norway modified after Larsen et al. (2018). The ultramafic complexes are indicated in green. This paper focuses on the Reinfjord Ultramafic Complex, which formed adjacent to gabbro and meta-sedimentary gneiss.

We focus on identifying and characterizing the primary magnetic minerals in the ultramafic rocks of the RUC. Petrophysical properties are used to determine if these rocks can represent a source of primary magnetization, which is stable in lower crustal to uppermost mantle settings.

2. Geology

2.1. Regional Setting

The SIP has an exposed area of more than 5,000 km^2 and an estimated minimum volume of ~17,000 km^3 of Ediacaran mafic and ultramafic rocks (Pastore et al., 2016; Pastore, Fichler, & McEnroe, 2018). The SIP was emplaced at approximately 570–560 Ma at depths of 25–35 km (Larsen et al., 2018; Roberts, 2007; Roberts et al., 2006). It is part of the Central Iapetus Magmatic Province and is composed of several ultramafic complexes including the Nordre Bumansfjord, Melkvann, Kvalfjord, and the Reinfjord complexes (Bennett et al., 1986; Larsen et al., 2018; Oosterom, 1954; Robins & Gardner, 1975; Yeo, 1984). The SIP is part of the Kalak Nappe Complex, classified as the Middle, or Upper Allochthon (Andréasson et al., 1998; Corfu et al., 2007; Gee et al., 2014; Larsen et al., 2018; Roberts, 1985; Siedlecka et al., 2004).

2.2. Local Geology

The RUC is located on the Øksfjord peninsula (Figure 1), which is dominated by layered gabbro complexes (Emblin, 1985). The RUC intruded near the contact between gabbro and garnet gneiss and covers an area of 25 km^2 (Figure 2; Bennett, 1972; Bennett, 1974; Larsen et al., 2018). The ultramafic cumulates comprise dunitic, wehrlitic, lherzolitic, and olivine pyroxenite compositions (Grant et al., 2016; Larsen et al., 2018; Robins & Gardner, 1975). Parent melts were ultramafic in composition and probably comprised picritic melts with 16–21 wt% MgO (Bennett et al., 1986; Grant et al., 2016; Larsen et al., 2018) or extreme dunitic melts with 40 wt% MgO according to some models (Griffin et al., 2013).

2.3. Rock Units

The RUC consists of three major ultramafic series: a lower layered series (LLS), an upper layered series (ULS), and a central series (CS). There is a marginal zone (MZ) where the ultramafic lithologies intruded gabbro or gneiss, resulting in hybrid zones where the hot ultramafic melts mixed with the host rocks at temperatures of at least 1400 °C (Bennett et al., 1986; Griffin et al., 2013; Larsen et al., 2018) and pressures of 6.8–9 kbar (Grant et al., 2016). A complete description of the lithologies can be found in Grant et al. (2016).

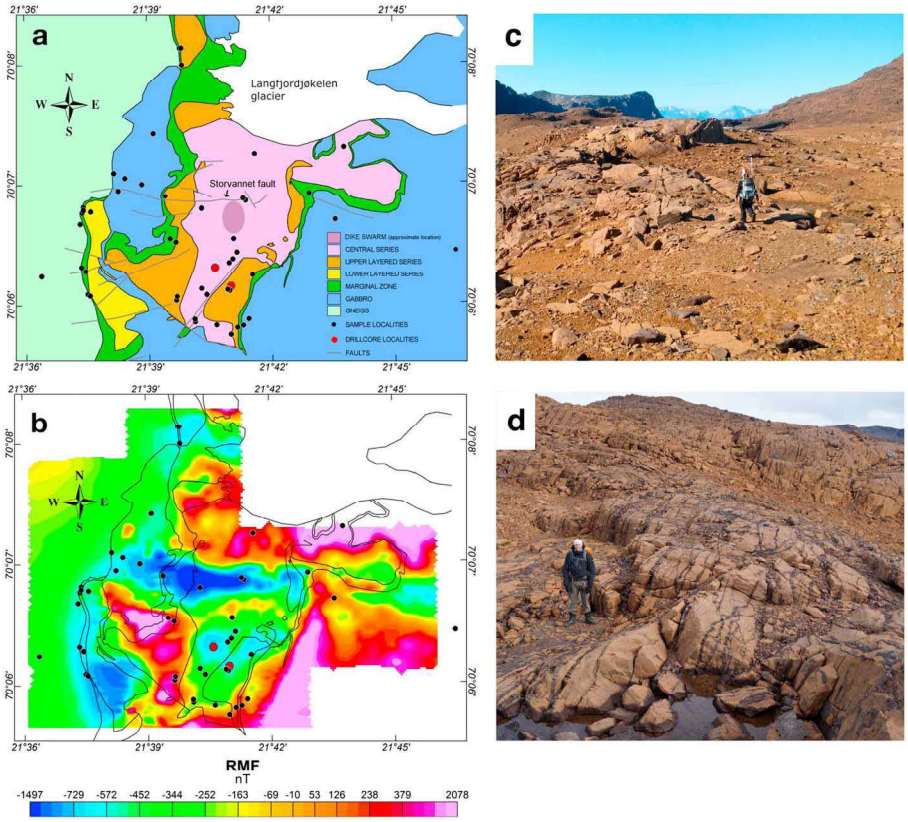

Figure 2. (a) Geological map of the Reinfjord Ultramafic complex (modified after Larsen et al., 2018). The sampling locations are indicated in black dots, and drill core locations are indicated by the red circles. Faults are indicated in gray (from Emblin, 1985). The shaded area in the center indicates the approximate location of a dike swarm where the density of dikes is higher than in the rest of the central series (CS). (b) High-resolution helicopter aeromagnetic map (SkyTEM surveys, 2011) showing the residual total magnetic intensity. The outlines of the contacts are shown in black, as well as the sample locations. Field images of the RUC show the superb exposure in the area of the (c) CS and (d) pyroxenite dikes.

The LLS is mapped as the oldest unit and contains a 300-m sequence of olivine ($Fo_{84.6–76.1}$), lherzolite, wehrlite, and olivine clinopyroxenite (Emblin, 1985; Grant et al., 2016). These rocks outcrop only on the western side of the intrusion (Figure 2) and are separated from the rest of the RUC by a 50- to 100-m-thick wall of gabbros that delaminated from the host rock gabbros. The ULS is dominated by wehrlitic cumulates and outcrops on both sides of the CS (Figure 2). The ULS has cyclic units consisting of a dunitic cumulate layer ($Fo_{85.1–77.4}$; Emblin, 1985) that gradually taper into wehrlitic cumulates. The later intrusion of the CS into the wehrlitic cumulates led to the assimilation of large volumes of the ULS under the formation of replacive dunites (Larsen et al., 2018). More than 50% of the surface outcrop of the RUC is CS, which consists of olivine cumulates (>90%) with less than 10% clinopyroxene. The compositions of the clinopyroxenes range from augite to diopside with has a xMg of 88.5 to 91.3 in the ULS and of 85.9–92.1 in the CS. The CS hosts a platinum group element-Cu-Ni mineralization (Grant et al., 2016; Iljina, 2012; Larsen et al., 2018; Schanche et al., 2012).

An extensive network of subvertical dikes can be traced throughout the mafic and ultramafic lithologies. The dikes intruded at temperatures up to 1450 °C (Yeo, 1984) and show several generations of emplacement with varying compositions, ranging from dunitic cumulate dikes, through pyroxenitic compositions to gabbroic pyroxene-hornblende-plagioclase rock types (Grant et al., 2016). The absence of chilled margins along the contacts of early ultramafic dikes intersecting RUC and their coarse-grained nature, even of centimeter-thin dikes, implies that the ultramafic rocks were still quite hot when the dikes were emplaced (Bennett et al., 1986; Emblin, 1985; Larsen et al., 2018).

The MZs have distinct mineral assemblages. The assemblage depends on the composition of the ultramafic cumulates, and the host rock at each location. Generally, the MZ is dominated by clinopyroxene and orthopyroxene, with smaller amounts of olivine and plagioclase (Emblin, 1985; Grant et al., 2016). In this paper,

we further subdivided the MZ depending on the adjacent host rock, gneiss (MZ_gneiss), or gabbro (MZ_gabbro).

Previous authors have reported local serpentinization in surface exposures of the ultramafic rocks (Emblin, 1985; Grant et al., 2016; Larsen et al., 2018). However, there is one area of pervasive serpentinization of the CS dunites, which is associated with a fault trending east-west at 70°07′N that crosscuts all formations (Figure 2), here termed the Storvannet fault. This fault zone likely provided a pathway for fluids, resulting in high degrees of serpentinization of the dunites ((Bennett et al., 1986; Emblin, 1985).

2.4. High-Resolution Aeromagnetic Survey

In 2011 SkyTEM Surveys conducted a high-resolution aeromagnetic helicopter survey over Reinfjord (Johnson, 2011; SkyTEM surveys, 2011), with a nominal terrain clearance of 30–40 m. The residual total magnetic intensity (RMF) map, calculated by subtracting the IGRF-2010 (Finlay et al., 2010) from the measured total magnetic intensity, is shown in Figure 2. The magnetic data processing involved low-pass filtering, leveling of the data, and correction for diurnal variation. Magnetic anomalies in the area have a range of −1,497 nT (below background) up to 2,078 nT.

The residual magnetic field over the CS formation varies from approximately −500 to 1,069 nT. The northern area of the CS corresponds with a magnetic high where the maximum RMF is 1,069 nT. The magnetic high in the center of the CS corresponds to a reported dike swarm (Grant et al., 2016), where there is an enhanced concentration of pyroxenite dikes (Figure 2). The southern part of the CS and the eastern part of the ULS correlate with a magnetic low, with an average RMF of approximately −500 nT. To the east, both the gabbro and the contact MZs correspond with magnetic highs. The gabbro to the east is associated with a magnetic anomaly high with a maximum amplitude of 1,791 nT. By contrast, the garnet gneiss, LLS, and associated contact MZs correspond to a magnetic anomaly low with a maximum amplitude of −1,000 nT below background. There is a distinct magnetic low, with a maximum field intensity of −1,496 nT, associated with the Storvannet fault and the associated heavily serpentinized rocks described above.

3. Methods

3.1. Sampling

Fifty-three sites were sampled during two field seasons. Site locations are shown on the geological map (Figure 2a), and geographic coordinates are included in the supporting information (S1). Samples were drilled and oriented in the field or collected as oriented blocks and drilled in the laboratory at Norwegian University of Science and Technology (NTNU). Cores were subsampled resulting in a total of 525 specimens of 2.2 cm long and 2.5 cm in diameter. Four deep drill cores were made in the area (Grant et al., 2016; Larsen et al., 2018). Two of these, RF3 and RF4, were subsampled for 142 specimens. Drill core RF3 is 348-m deep, with the upper 100 m of ULS rock, and the remaining 248 m is CS. RF4 is 391-m deep and consists of 351-m CS rock and 40 m of rocks similar to the MZ_gabbro (Grant et al., 2016). Samples from RF3 and RF4 cores lack declination information.

3.2. Microscopy

Thin sections were examined using transmitted and reflected light microscopy. Transmitted light observations were compared to modes reported in previous studies from the same rock units (Bennett et al., 1986; Emblin, 1985; Grant et al., 2016; Larsen et al., 2018) to determine if our samples are representative. Samples were inspected for serpentinization of the olivine and pyroxene, identified in transmitted light by a mesh-like structure (Maffione et al., 2014). Rough estimates of serpentine mineral content were made using ImageJ by thresholding based on gray scale value (Heilbronner & Barret, 2014). Oxides and sulfides were identified in reflected light.

3.3. Petrophysical Measurements

Density measurements of 667 specimens were made using a Mettler Toledo ML104 scale with a density kit. To fill pore space, specimens were first soaked in water for a minimum of 24 hr. The sample mass in air, and the mass in water, was measured and used to calculate sample density and volume.

Measurements of natural remanent magnetization (NRM) were made with an AGICO JR6 spinner magnetometer at NTNU. The deep drill core samples were measured in a 2G cryogenic magnetometer at the

Institute for Rock Magnetism at the University of Minnesota. The magnetic susceptibility κ (SI) was measured using a Sapphire susceptibility bridge with a field of 80 A/m at NTNU. To compare susceptibility and NRM values, all sample data were volume normalized.

Temperature-susceptibility measurements on rock powders from −194 to +700 °C in a field of 200 A/m were acquired using an AGICO MFK1A Kappabridge. For further characterization of the magnetic carriers, a Princeton Measurement Corp Vibrating Sample Magnetometer was used. Hysteresis loops were measured in a maximum field of 1 T, providing the parameters saturation magnetization (M_s), remanent saturation magnetization (M_{rs}), and coercivity (H_c), and backfield remanence curves provide the parameter coercivity of remanence (H_{cr}). The ratios between the properties M_{rs}/M_s and H_{cr}/H_c were used to evaluate the magnetic mineralogy and give insight into domain states.

4. Results

4.1. Transmitted Light Microscopy

Thin sections of the different lithologies were studied using transmitted light microscopy to confirm the reported mineralogy and assess the degree of alteration. Micrographs for each formation are shown in Figure 3. The opaque grains are discussed in the next section.

The CS consists of olivine (>90%) and minor clinopyroxene (Figure 3a). The olivine has varying grain sizes, from >1 mm to smaller grains (~100–200 μm). In the ULS there are similar grain sizes of olivine (15–40%) with more abundant clinopyroxene (60–85%), in agreement with Grant et al. (2016). Clinopyroxene grains commonly contain exsolution lamellae of orthopyroxene. Figure 3c shows a pyroxenite dike from the ULS. This sample contains large magmatic amphibole, clinopyroxene and orthopyroxene, and small plagioclase grains. Fine-grained opaques are found in the matrix and in pyroxene (exsolution). The LLS samples have varying modal abundances, with some samples consisting mainly of orthopyroxene and clinopyroxene (Figure 3d), while others contain mainly olivine. There are varying amounts (1–3%) of large interstitial opaque grains between the olivine grains in the CS, ULS, and LLS samples. In the LLS the olivine-rich samples contain more opaques than the more pyroxene-rich rocks. Some olivine grains in the ultramafic formations show minor serpentinization (Figure 3a).

The MZ_gneiss samples, formed in contact with the garnet gneiss, consists of clinopyroxene, orthopyroxene, and plagioclase (Figure 3e). The MZ_gabbro (Figure 3f) samples mainly consist of clinopyroxene, orthopyroxene, and olivine, and commonly have more clinopyroxene and olivine, and less plagioclase than the MZ_gneiss samples. The clinopyroxene in MZ samples contains exsolution lamellae, which form both blades and needles of orthopyroxene and opaques.

The gabbro host rock samples of the RUC contain olivine, clinopyroxene, plagioclase, orthopyroxene, amphibole, and opaques. The samples from the western side of the intrusion contain more clinopyroxene than the eastern samples. Opaque grains are abundant in all gabbro samples.

The gabbro host rock samples of the RUC contain olivine, clinopyroxene, plagioclase, orthopyroxene, amphibole, and opaques. The samples from the western side of the intrusion contain more clinopyroxene than the eastern samples. Opaque grains are abundant in all gabbro samples. The serpentinized samples from the Storvannet fault area (Figure 3h) contain abundant serpentinite minerals. In addition, relic olivine rafts of CS dunite protolith are present. Image analysis for this sample yields a serpentinization degree of ~70%.

4.2. Reflected Light Microscopy

Reflected light microscopy was used to identify the dominant oxides and sulfides. Common to all ultramafic formations are large chrome-spinel and ilmenite grains (Figures 4a–4c). The nomenclature of spinel group minerals in the literature is not consistent; here, we use the general term chrome-spinel to describe Fe- and Cr-rich spinel phases. The large chrome-spinel grains usually are in association with olivine, and, as expected, are most abundant in the olivine-rich CS rocks. In the ULS and LLS the chrome-spinel grains are most abundant in the samples that contain the most olivine. In the CS drill core samples, some chrome-spinel grains show a clear zonation with a more iron-rich rim (Figure 4d). Locally, the ultramafic rocks can contain abundant sulfides (Figure 4e). We observed chalcopyrite, commonly in assemblage with pyrrhotite, pyrite, and pentlandite.

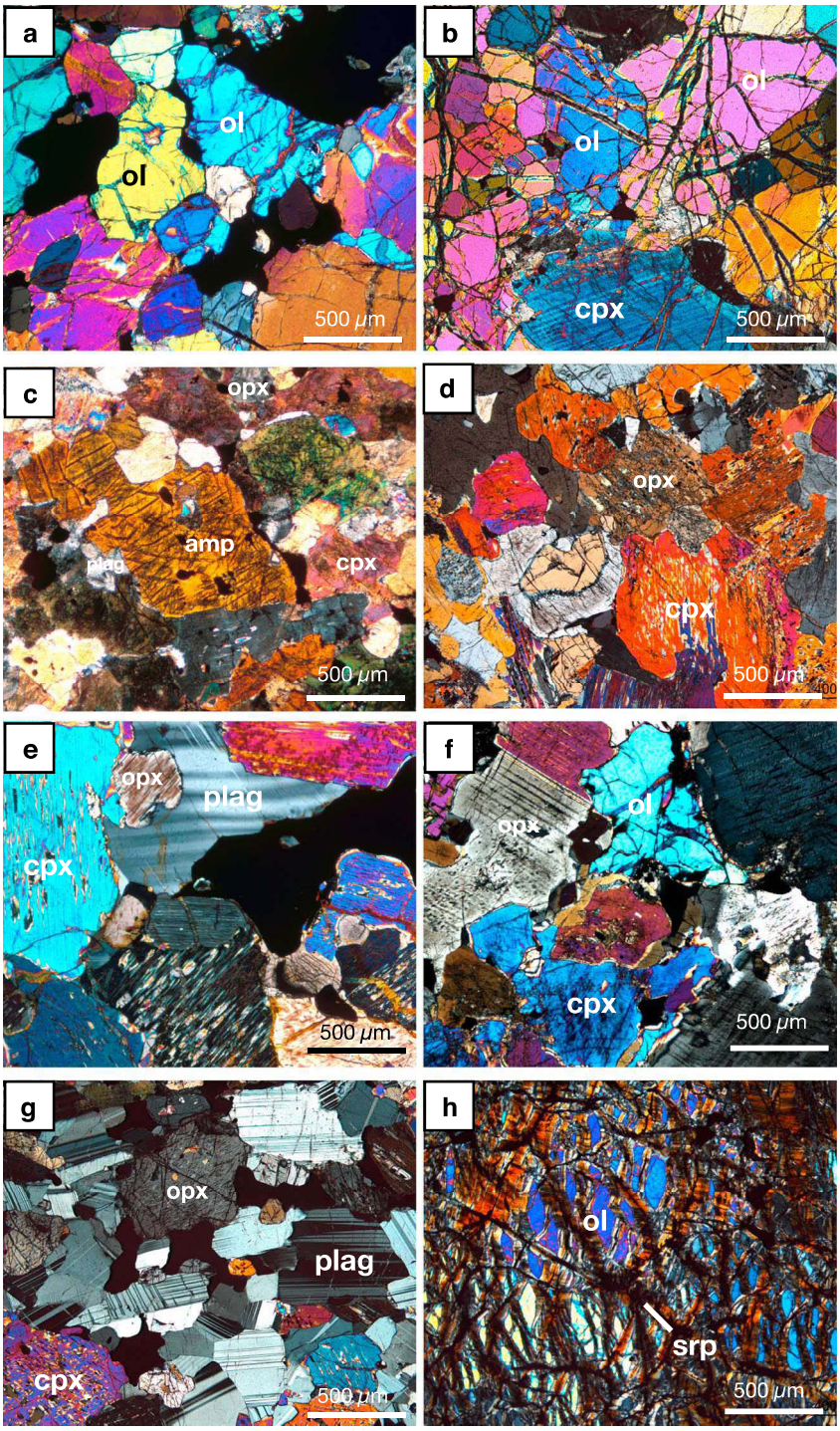

Figure 3. Micrographs in transmitted light of a representative sample all formations: (a) central series (CS), (b) upper layered series (ULS), (c) pyroxenite dike, (d) lower layered series (LLS), (e) MZ_gneiss, (f) MZ_gabbro, (g) Gabbro, and (h) serpentinite. ol: olivine; srp: serpentinite; cpx: clinopyroxene; opx: orthopyroxene; plag: plagioclase; amp: amphibole.

In many of the chrome-spinel grains exsolution microstructures are present (Figures 4b and 4c). The exsolved phase ranges is size from >10 μm to submicron and occurs randomly distributed as irregular, sub-rounded blebs. Similar textures in chrome-spinel are reported by other authors (Colas et al., 2016; Eales et al., 1988; Loferski & Lipin, 1983; Ramdohr, 1980).

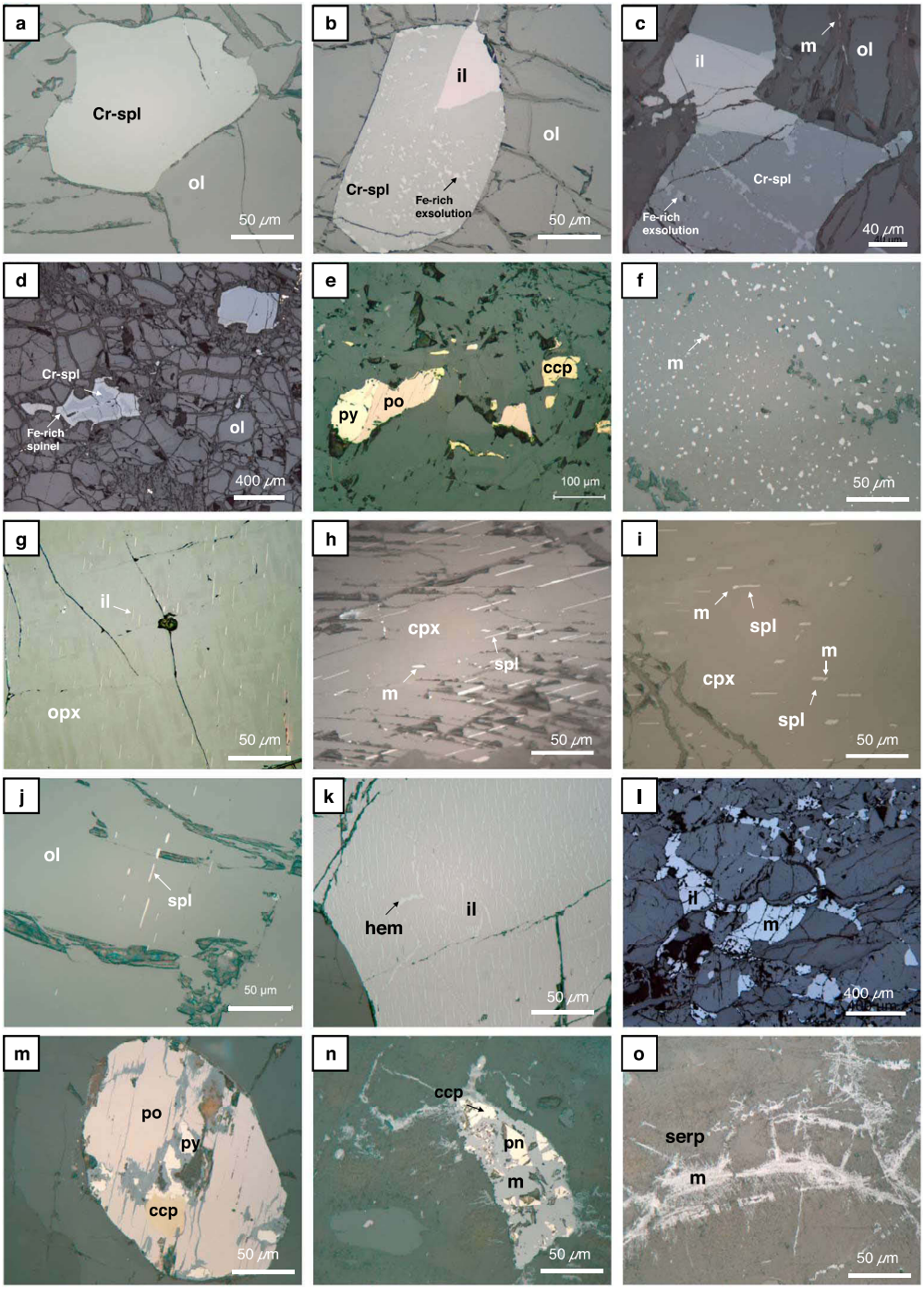

Figure 4. Reflected light images of (a) homogenous chrome-spinel and (b and c) chrome-spinel and ilmenite from central series (CS) surface rocks. The chrome-spinel contains exsolution microstructures of a more iron-rich phase. (d) Chrome-spinel with an iron-rich rim from CS drill core samples. (e) Pyrite, pyrrhotite, and chalcopyrite in the CS surface samples. (f) Magnetite in a pyroxenite dike sample. (g) Exsolution of ilmenite lamellae from orthopyroxene in MZ_gneiss rocks. Exsolution of magnetite and spinel from clinopyroxene in (h) upper layered series (ULS) and (i) MZ_gabbro rocks. (j) Spinel exsolution from olivine in CS rocks. (k) Hemo-ilmenite in gabbro rocks, (l) magnetite, and ilmenite in gabbro rocks. (m) Pyrrhotite-chalcopyrite-pyrite in gabbro rocks. (n) Pentlandite-chalcopyrite-magnetite assemblages in CS serpentinite. (o) Magnetite in serpentinite veins in CS serpentinite. m: magnetite; il: ilmenite; hem: hematite; po: pyrrhotite; py: pyrite; ccp: chalcopyrite; Cr-spl: chrome-spinel; spl: spinel; pn: pentlandite; serp: serpentinite.

The chemical composition of the exsolution microstructures and host chrome-spinel in CS rocks is reported by Pastore, McEnroe, ter Maat, et al. (2018). The composition is obtained by electron microprobe analysis and is $[(Fe^{2+}_{0.94}Mg_{0.07}Ni_{0.01})_{1.02}(Fe^{3+}_{1.33}Cr_{0.46}Al_{0.15}Ti_{0.03})_{1.97}O_4]$ for the exsolution microstructures and $[(Fe^{2+}_{0.76}Mg_{0.25})_{1.01}(Fe^{3+}_{0.46}Cr_{0.74}Al_{0.75}Ti_{0.03})_{1.97}O_4]$ for the host chrome-spinel. The host chrome-spinel contains more Cr and Al, and the exsolved phase is more Fe-rich. Due to the typical small size of the exsolution most analyses are overlap analyses and this results in an underestimation of the iron content of the exsolved phase.

In many of the silicates in the RUC and host rocks exsolution of oxides is present. Some olivine grains contain minor exsolution of spinel (Figure 4j). The orthopyroxene grains contain exsolution lamellae of ilmenite (Figure 4g). In clinopyroxene there are exsolution lamellae of ilmenite, exsolved blades of chrome-spinel with magnetite rods typically at the end of the blade (Figures 4h and 4i). The ULS pyroxenite dike has abundant fine-grained spinels in the matrix (Figure 4f). Some of the MZ samples contain discrete magnetite grains with minor spinel exsolution and rare oxidation exsolution of ilmenite.

The layered gabbro contains variations in oxide and sulfide mineralogy, and these are strongly dependent on geographic location. Magnetite and ilmenite are present in the southern gabbro samples (Figure 4l). Hemoilmenite is found in the more northern samples (Figure 4k). On the northwestern side of the intrusion hemoilmenite is found together with pyrrhotite (Figure 4m), which is an unusual assemblage.

Some ultramafic samples show evidence of minor serpentinization (Figures 4c and 4d) with occasional formation of magnetite in the serpentinite veins (Figure 4c). However, in samples with only minor serpentinization, little or no magnetite was observed in the veins.

In the serpentinite samples magnetite is common in the serpentinite veins and in association with large magnetite-pentlandite-chalcopyrite grains (Figure 4n). These samples also contain relic olivine grains. The magnetite-pentlandite-chalcopyrite assemblage is only found in the serpentinite samples from the Storvannet fault; this assemblage is not observed in samples with only minor serpentinization.

4.3. Petrophysical Data: NRM, Susceptibility, Density

There is notable variation in the magnetic and petrophysical properties (NRM, susceptibility, and density); data tables for the 667 samples are given in Table S1. The box and whisker plots of the NRM, susceptibility, and density are shown in Figure 5; the values for mean, median, and the bounding box are given in Table 1. Both susceptibility and NRM are plotted on a logarithmic scale. Each box encloses the middle 50% of the samples with the median value shown as a black line, and arithmetic mean as red line. The whiskers show the minimum and maximum of the distribution.

NRM values for the RUC range from 0.002 to 26.4 A/m, with a median of 0.77 A/m. Two extreme outliers are excluded, which are considered contaminated due to high (>3 standard deviations above mean) NRM values and directions inconsistent with other specimens of the same site. The range in susceptibility values is from 0.0002 to 0.07 SI, and a median of 0.007 SI. Density values range from 2.55 to 3.42 g/cm^3, with a median of 3.21 g/cm$^{3.}$ Commonly, the NRM and susceptibility values have a distribution closer to lognormal than linear, which results in a higher mean value than the median value. Below data for each formation are discussed.

4.3.1. NRM

CS samples from the deep drill cores have lower NRM values (from 0.08 to 5.3 A/m) than the surface samples (0.1 to 22 A/m). The median values of the CS drill core samples are 0.38 and 1.2 A/m for the CS surface samples.

As with the CS, the ULS surface samples have higher median NRM values than the ULS drill core, at 0.53 and 0.38 A/m, respectively. The range in NRM values is similar for the ULS surface (from 0.02 to 6.5 A/m) and drill core samples (from 0.1 to 5.3 A/m). The pyroxenite dike samples have a large range with NRM values from 1.2 to 26.4 A/m, with a median of 4 A/m. The LLS samples are less strongly magnetic, with NRM values from 0.007 to 3.7 A/m and a median of 0.60 A/m.

The range in NRM values of MZ samples is large, from 0.002 to 11.6 A/m, with a median of 0.58 A/m. By contrast, the gabbro has a smaller range from 0.02 to 3.7 A/m, with a median of 0.9 A/m.

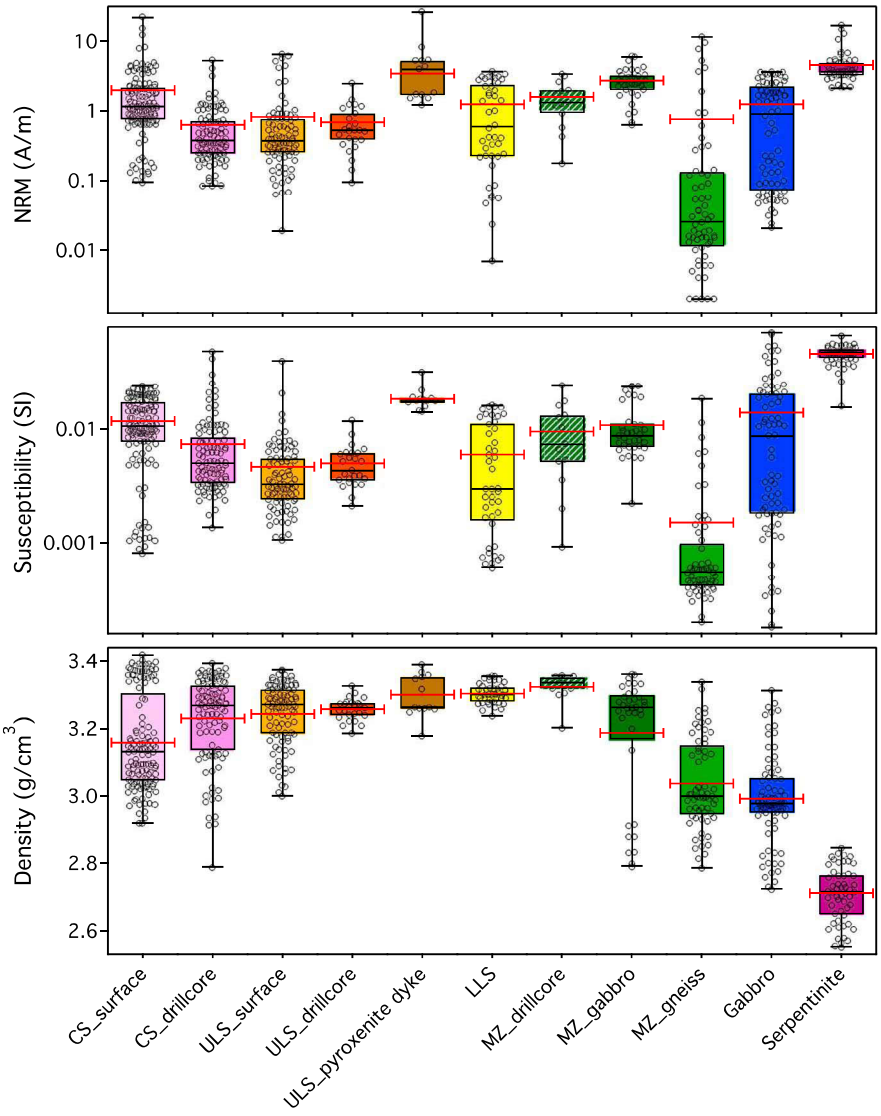

Figure 5. Box- and whisker plots of density, natural remanent magnetization (NRM), and susceptibility values by formation, and by location, surface, and drill core. The MZ is further subdivided by the contact unit host rock. The serpentinized samples from the Storvannet fault zone are plotted separately. Plots show the 3, 25, 50 (black line, median), 0, and 100 percentile and the arithmetic mean (red line). Samples are plotted as black circles. One outlier from the CS and a pyroxenite dike were excluded, though in the supporting information.

The strongly serpentinized dunite samples from the Storvannet fault zone have NRM values from 2.1 to 16.9 A/m, with a median of 3.7 A/m. Such values are much higher than those of the CS surface and drill core rocks.

4.3.2. Susceptibility

There is a large variation in susceptibility values for the RUC. These differences are most prominent between the surface and drill core samples for certain formations.

For the CS surface and drill core samples, the volume normalized susceptibility values range from 0.0008 to 0.024 SI and from 0.0014 to 0.048 SI, respectively. Despite higher extreme values in the drill core samples, the CS_surface samples yield higher median values than the CS_drillcore, at 0.011 SI and 0.0050 SI, respectively. In the ULS, susceptibility values for the surface and drill core samples are similar with a range of 0.0011 to 0.0205 SI. The median values are close at 0.0033 SI for the surface samples and 0.0043 SI for the drill core samples. The CS and ULS display the opposite trend: the CS surface samples have higher values than the CS drill core, whereas the ULS_surface samples have lower susceptibility values than the drill core. The median of the CS surface samples is twice that of the CS_drillcore, ULS_surface, and ULS_drillcore sample sets.

Table 1
Statistical Distributions of NRM (A/m), Susceptibility (SI), and Density (g/cm^3)

NRM (A/m)	Mean	Min	25%	Median	75%	Max
CS surface[a] (131)	1.999	0.095	0.764	1.166	2.182	22.022
CS drill core (104)	0.640	0.084	0.247	0.379	0.723	5.304
ULS surface (87)	0.823	0.019	0.256	0.376	0.773	6.511
ULS drill core (25)	0.690	0.095	0.390	0.531	0.920	2.478
ULS pyroxenite dyke[a] (13)	5.241	1.225	1.698	3.963	5.260	26.389
LLS (44)	1.255	0.007	0.226	0.601	2.312	3.672
MZ_ALL (113)	1.498	0.002	0.019	0.575	2.485	11.575
MZ_drillcore (13)	1.598	0.178	0.938	1.327	2.001	3.400
MZ_gabbro (36)	2.763	0.636	2.009	2.665	3.233	6.003
MZ_gneiss (64)	0.766	0.002	0.012	0.026	0.130	11.575
Gabbro (78)	1.246	0.021	0.076	0.908	2.193	3.648
Serpentinite (54)	4.618	2.127	3.273	3.659	4.873	16.847
Susceptibility (SI)	**Mean**	**Min**	**25%**	**Median**	**75%**	**Max**
CS surface[a] (132)	0.0118	0.0008	0.0078	0.0107	0.0173	0.0242
CS drill core (103)	0.0074	0.0014	0.0034	0.0050	0.0082	0.0483
ULS surface (88)	0.0047	0.0011	0.0024	0.0033	0.0055	0.0398
ULS drill core (25)	0.0050	0.0021	0.0035	0.0043	0.0062	0.0118
ULS pyroxenite dyke[a] (13)	0.0185	0.0141	0.0171	0.0176	0.0184	0.0318
LLS (44)	0.0060	0.0006	0.0016	0.0030	0.0111	0.0162
MZ_ALL (113)	0.0054	0.0002	0.0005	0.0018	0.0083	0.0243
MZ_drillcore (13)	0.0096	0.0009	0.0051	0.0074	0.0133	0.0243
MZ_gabbro (36)	0.0108	0.0022	0.0070	0.0088	0.0111	0.0240
MZ_gneiss (64)	0.0015	0.0002	0.0004	0.0006	0.0009	0.0186
Gabbro (75)	0.0141	0.0002	0.0018	0.0087	0.0206	0.0710
Serpentinite (54)	0.0460	0.0157	0.0423	0.0473	0.0501	0.0669
Density	**Mean**	**Min**	**25%**	**Median**	**75%**	**Max**
CS surface[a] (135)	3.158	2.920	3.047	3.132	3.298	3.418
CS drill core (104)	3.230	2.790	3.138	3.269	3.328	3.394
ULS surface (95)	3.244	3.001	3.186	3.272	3.317	3.375
ULS drill core (25)	3.258	3.186	3.240	3.262	3.276	3.327
ULS pyroxenite dyke[a] (13)	3.302	3.179	3.260	3.292	3.358	3.390
LLS (44)	3.304	3.238	3.281	3.302	3.321	3.356
MZ_ALL (113)	3.111	2.787	2.960	3.127	3.283	3.362
MZ_drillcore (13)	3.324	3.203	3.320	3.337	3.352	3.358
MZ_gabbro (36)	3.187	2.793	3.184	3.264	3.297	3.362
MZ_gneis (64)	3.037	2.787	2.948	3.000	3.147	3.339
Gabbro (82)	2.992	2.725	2.952	2.978	3.053	3.313
Serpentinite (54)	2.712	2.553	2.657	2.720	2.769	2.847

Note. Number of samples in parentheses. NRM, natural remanent magnetization.
[a]Excluding 1 outlier.

The LLS susceptibility values range over 2 orders of magnitude from 0.0006 to 0.016 SI and have a median of 0.0030 SI. Samples from the layered gabbro show a similarly large range from 0.0002 to 0.071 with a median of 0.014 SI. The MZ samples have a susceptibility value range from 0.0002 to 0.024 SI, with a median value of 0.0018 SI.

4.3.3. Density

A total of 667 samples were measured for density. The lowest median density values in the data set are recorded in the serpentinite samples, while the highest values are in the MZ_drillcore samples. The mean densities measured for the ultramafic formations are higher than the mean densities of serpentinized dunites (2.83 g/cm^3) and harzburgites (2.79 g/cm^3) reported in mantle material from the Leka Ophiolite Complex (Michels et al., 2018).

The density range in the 135 CS_surface samples is 2.92 to 3.42 g/cm^3, with a median value of 3.13 g/cm^3. The density of the 104 CS_drillcore samples ranges from 2.79 to 3.39 g/cm^3, with a median of 3.27 g/cm^3.

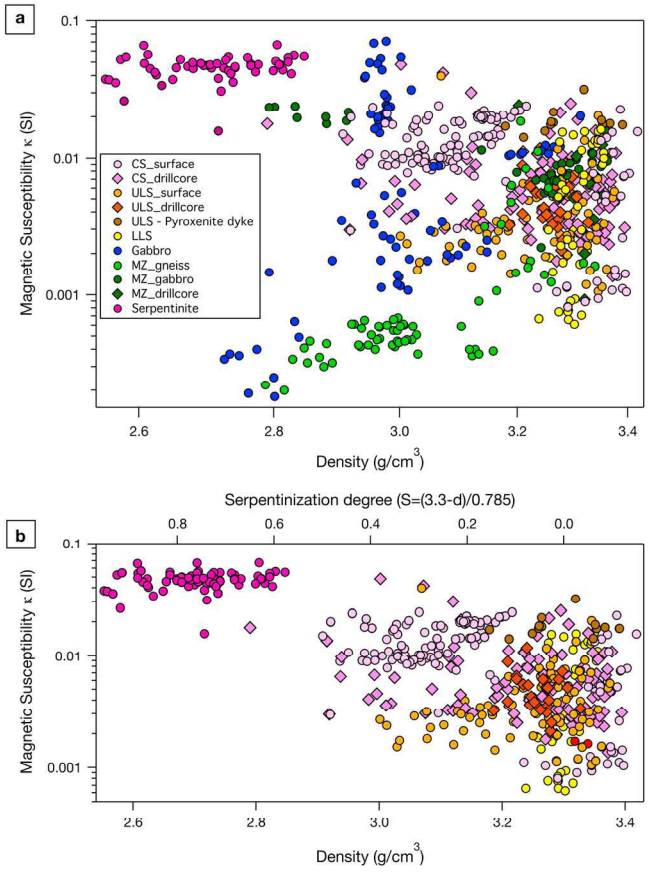

Figure 6. (a) Density versus susceptibility for all formations and (b) only the ultramafic samples. For the ultramafic samples the calculated serpentinization degree is added on the top axis.

The distribution of data points on the box plot (black circles; Figure 5) is bimodal for the surface and drill core samples. There is a cluster of high-density samples in the surface samples above 3.3 g/cm^3, and in the drill core samples above 3.2 g/cm^3. Locally, in the drill core, there are crosscutting centimeter-sized fractures with serpentinite minerals (Grant et al., 2016), which may be the explanation of the lowest density values.

The 95 ULS surface and drill core (25) samples have a relatively small range in density with ULS_surface sample densities from 3.00 to 3.38 g/cm^3 and ULS_drillcore samples 3.19 to 3.33 g/cm^3. The median value of the ULS_surface samples (3.27 g/cm^3) is similar to that of the ULS_drillcore samples (3.26 g/cm^3). The LLS samples also have a narrow range in density, from 3.24 to 3.36 g/cm^3 with a median of 3.30 g/cm^3.

The MZ and gabbro samples show large ranges in density from 2.79 to 3.36 g/cm^3, and from 2.73 to 3.31 g/cm^3, respectively. The median density value of the MZ samples is 3.13 g/cm^3, and 2.98 g/cm^3 for the gabbro samples.

The density values of the serpentinite samples reflect the variable, but generally high, degree of serpentinization. The total range is from 2.55 to 2.85 g/cm^3, significantly lower than the densities of unaltered CS samples, which have a median of 3.13 g/cm^3. The degree of serpentinization of the rocks from the Storvannet fault, calculated after Miller and Christensen (Miller & Christensen, 1997), varies from 58 to 95%.

4.4. Susceptibility Versus Density

Covariation of density and susceptibility can result from magmatic processes, such as later sulfide mineralization, or secondary alteration, such as serpentinization. We would not expect covariance in the pristine rocks, which have not been subjected to these secondary processes. To evaluate for these processes, magnetic susceptibility (SI) and density (g/cm^3) are plotted for all formations in Figure 6a. In addition, an expanded view containing only the ultramafic formations (CS, ULS, and LLS) is shown in Figure 6b and on a linear scale in Figure S1.

There is no strong correlation between density and susceptibility. The CS samples show a small increase in susceptibility with decreasing density, which may result from variable but limited serpentinization (e.g., Figures 4c and 4d). CS surface samples with a density above 3.2 g/cm^3 show a large range in susceptibility. The ULS samples show no clear trend. The LLS samples have a narrow range in density and a large range in susceptibility. Samples from three of the four MZ_gabbro sites cluster at high densities (3.2–3.3 g/cm^3), and the remaining site plots at lower density and higher susceptibility values. The MZ_gneiss samples show a slight increase in susceptibility with increasing density. The gabbro samples show a large range in susceptibility, with the lowest values corresponding to low density values. The serpentinite samples have similar susceptibility values for a wide range in densities.

To determine which densities best represent the pristine ultramafic rocks, we compared our measured properties to estimates of serpentinization degree from thin section analysis, widely applied calculations using density values, and the theoretical densities of unaltered ultramafic rocks.

For ease of viewing, only ultramafic formations are plotted in Figure 6b, with the serpentinization degree (top axis) after Miller and Christensen (1997), which is based on density and assumes a maximum value of 3.3 g/cm^3 for unaltered peridotite and ultramafic rocks (their Figure 8). Using their calculation, our samples with densities above 3.3 g/cm^3 (38% of ultramafic samples) plot in an area of negative serpentinization degree, clearly an unphysical result.

We compared our measured densities to theoretical densities of our ultramafic rocks. Theoretical densities were calculated based on bulk composition using macros by Hacker and Abers (2004) and the composition estimates

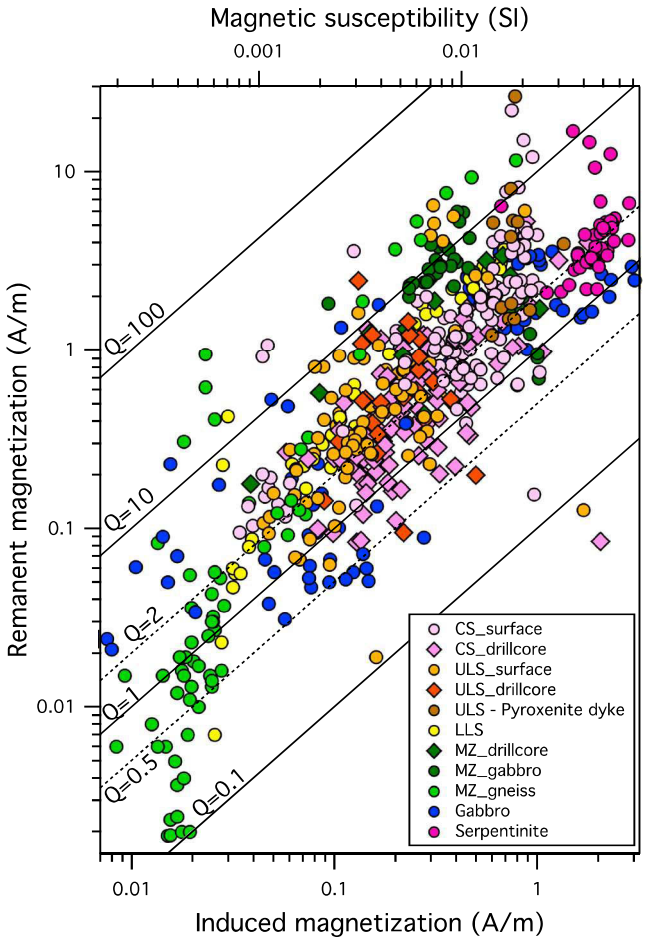

Figure 7. Natural remanent magnetization (NRM) versus induced magnetization in A/m. Susceptibility is shown on the top axis. The black lines represent an equal Q value (remanent/induced magnetization), for the ratios $Q = 100$, 1, 0.1. The dashed lines represent the ratios $Q = 0.5$ and $Q = 2$.

from Grant et al. (2016) and Emblin (1985) for the ultramafic formations (CS, ULS, and LLS). The olivine composition varies from $Fo_{84.6–76.1}$ in the CS samples and $Fo_{85.1–77.4}$ in the ULS. The clinopyroxene is diopside to augite with xMg 85.9–92.1 for the CS and xMg 88.5–91.3 in the ULS. Most orthopyroxenes range in xMg from 0.83 to 0.87 in both ULS and LLS (Grant et al., 2016). For the minimum theoretical density, the estimated ratio ol:cpx:opx:spl of 0.905:0.009:0:0.005 (Emblin, 1985) is used for the CS and 0.79:0.13:0.08:0 for the ULS and LLS. These compositions give a minimum density of 3.42 g/cm^3 for CS and 3.40 g/cm^3 for ULS and LLS rocks. These values are slightly higher than the maximum measured densities of 3.42, 3.39, and 3.36 g/cm^3 for the CS, ULS, and LLS respectively.

4.5. NRM Versus Susceptibility and Induced Magnetization

To assess the contribution to magnetic anomalies from lithologies similar to the RUC, the Koenigsberger ratio, commonly referred to as the Q value, is evaluated. The Q value is the ratio of the NRM to the induced magnetization (M_i in A/m) given by $M_i = \kappa \times H$, where κ is volume-corrected susceptibility in SI units and H is the local Earth's field, here 42.5 A/m for Reinfjord (IGRF-2012, Thébault et al., 2015). In Figure 7 NRM is plotted against susceptibility (top axis) and M_i (bottom axis) with lines of constant Q value.

The samples of the RUC show an overall positive trend, whereby NRM increases with increasing susceptibility (or M_i). Of the samples, 87% plot above the line $Q = 1$, and 63% of the samples have a Q value higher than 2. This observation indicates the contribution the NRM to in situ magnetization is greater than that of the induced magnetization. However, to interpret the influence of the NRM on the anomaly, it is essential to know the volume and extent of the regions of coherent magnetization (Carporzen et al., 2006; Clark, 2014; Lillis et al., 2010; McEnroe et al., 2018; Purucker & Clark, 2011). The vector average of the Q value (Q_v, contrasted with scalar or nominal Q_n) is calculated to take into account variation in NRM directions and intensity (Brown & McEnroe, 2008; Dunlop et al., 2010; McEnroe & Brown, 2000).

The CS surface samples show similar Q values (mean $Q_n = 5.1$, $Q_v = 3.3$) to those of the ULS ($Q_n = 4.8$, $Q_v = 4.2$) and LLS ($Q_n = 4.9$ and $Q_v = 4.5$). The CS and ULS drill core samples only have inclination information and yield scalar Q values of 2.0 and 3.2, respectively. The pyroxenite dike samples have a large range in NRM and a limited distribution of susceptibilities, yielding $Q_n = 7.3$ and $Q_v = 7.0$. The MZ_gneiss samples have a large range in both NRM and susceptibility values, resulting in high Q_n and Q_v ratios of 12.0 and 11.4, respectively. The host gabbro samples have a Q_n of 2.1 and Q_v of 0.8, whereas the MZ_gabbro samples have higher ratios of Q_n of 5.5 and Q_v of 5.0. The serpentinite samples have the highest susceptibility values of the entire data set and lower ratios than the ultramafic rocks with Q_n of 2.3 and Q_v of 1.5. Less coherency in NRM directions can be due to both positive and negative inclinations being present and a high variability in declination. This is also true for the ultramafic surface samples where minor serpentinization results in greater variation in NRM direction.

The vectorially averaged Q_v values provide a good estimate of the influence of remanence on the magnetic anomalies. Except for the layered gabbros all formations have Q_v values over 2, which indicate that the remanent dominates the magnetic anomalies in the RUC, even when the dispersion of remanent directions is considered.

4.6. Hysteresis Properties

Magnetic domain states and consequent remanence intensity and stability can be inferred from hysteresis measurements, which can be expressed concisely on a Day plot (Day et al., 1977). This diagram displays the ratio of saturation remanent magnetization to saturation magnetization (M_{rs}/M_s) against that of

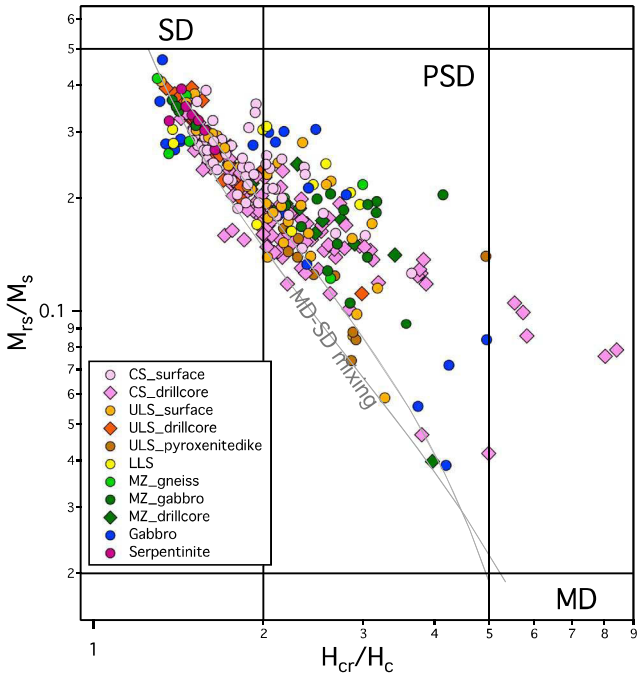

Figure 8. Day plot (Day et al., 1977) with ratio M_{rs}/M_s as a function of H_{cr}/H_c ratios. Mixing lines and single-domain (SD), pseudo-single domain (PSD), and multidomain (MD)regions after Dunlop (2002).

coercivity of remanence to coercivity (H_{cr}/H_c). Positions on the Day plot reflect magnetic switching behavior (averaged over the entire specimen), which is in turn a function of domain state. Domain state inferences from the Day plot are not definitive, as factors such as grain size distributions, mineralogy, and compositional variations also affect the position on the plot (Paterson et al., 2018; Roberts et al., 2014; Roberts et al., 2018). However, the relative positions of samples from a single data set can suggest trends reflecting variations in the magnetic carriers. Samples from the RUC are presented on a Day plot in Figure 8, with mixing lines and boundaries for single-domain (SD), pseudo-single domain (PSD), and multidomain (MD) behavior in magnetite after Dunlop (2002).

The RUC samples plot along the MD-SD mixing lines with 48% in the PSD region. None plot in the MD region or have an M_{rs}/M_s ratio above 0.5. Of the ultramafic formations, the ULS drill core samples plot closest to the SD limit, followed by the CS and ULS surface samples and the serpentinites. Compared to the surface specimens, the CS drill core samples have a larger proportion that do not approach end-member SD behavior and are those that plot closest to the MD region. By contrast, the ULS surface and drill core specimens show a wide and overlapping range of magnetic behavior that ranges from near ideal SD well into the PSD region. The LLS samples have similar M_{rs}/M_s values but higher H_{cr}/H_c than the CS and ULS surface samples. All ULS pyroxenite dike samples plot in the PSD region.

The MZ samples show a high degree of variability, with most samples plotting in the PSD region and others approaching ideal SD behavior. The MZ rocks, which formed in contact with gneiss, have a greater proportion that plot near ideal SD behavior. The MZ samples formed in association with gabbro (including the drill core samples) have a larger proportion in the PSD region. The samples plot close to the MD-SD mixing lines near the SD region and deviate from it further into the PSD region.

The gabbro samples show a large range in M_{rs}/M_s ratios with some samples plotting very close to the SD region and other samples plotting close to the MD region. This range of behavior reflects the mixed mineralogy of the gabbro: samples containing solely magnetite plot closer to the MD region, and those containing mainly hemo-ilmenite and pyrrhotite have hysteresis parameters plotting near to the SD field.

4.7. Curie Temperatures

Measurements of Curie temperatures (T_c) can provide diagnostic information about the mineralogy and presence of impurities in the magnetic phase(s) in a sample and complement microscopy observations. Mass-normalized temperature susceptibility curves from −190 to 700 °C are shown in Figure 9 for each formation of the RUC. The T_c was estimated using the point of maximum descent (Tauxe, 1998). All measurements were made in argon to minimize oxidation; however, all but one analysis were irreversible, indicating some alteration occurred during heating.

Temperature susceptibility curves for three CS samples with high densities (3.38, 3.37, and 3.34 g/cm^3) are shown in Figures 9a–9c, respectively. Though the densities are similar, these samples have a wide range in bulk susceptibility values from high (0.016 SI; Figure 9a), intermediate (0.005 SI; Figure 9b) to low (0.0012 SI, Figure 9c). The high- and intermediate-susceptibility samples (Figures 9a and 9b) show a low-temperature transition around −150 °C, the Verwey transition in magnetite (Verwey, 1939). The transition is not sharp, which indicates some degree of oxidation or cation substitution. Its occurrence indicates there is coexisting near-end-member magnetite because the Verwey transition is suppressed by small degrees of cation substitution (e.g., $x > 0.04$ titanium; Kakol et al., 1992). These specimens also display an increase in susceptibility from ~ −100 to +200 °C followed by a gradual decrease until the Curie temperature. By contrast, the third curve (Figure 9c) does not show a low-temperature transition, indicating that there is little near-end-member magnetite, and lacks the enhancement of susceptibility up to 200 °C. The T_c of these

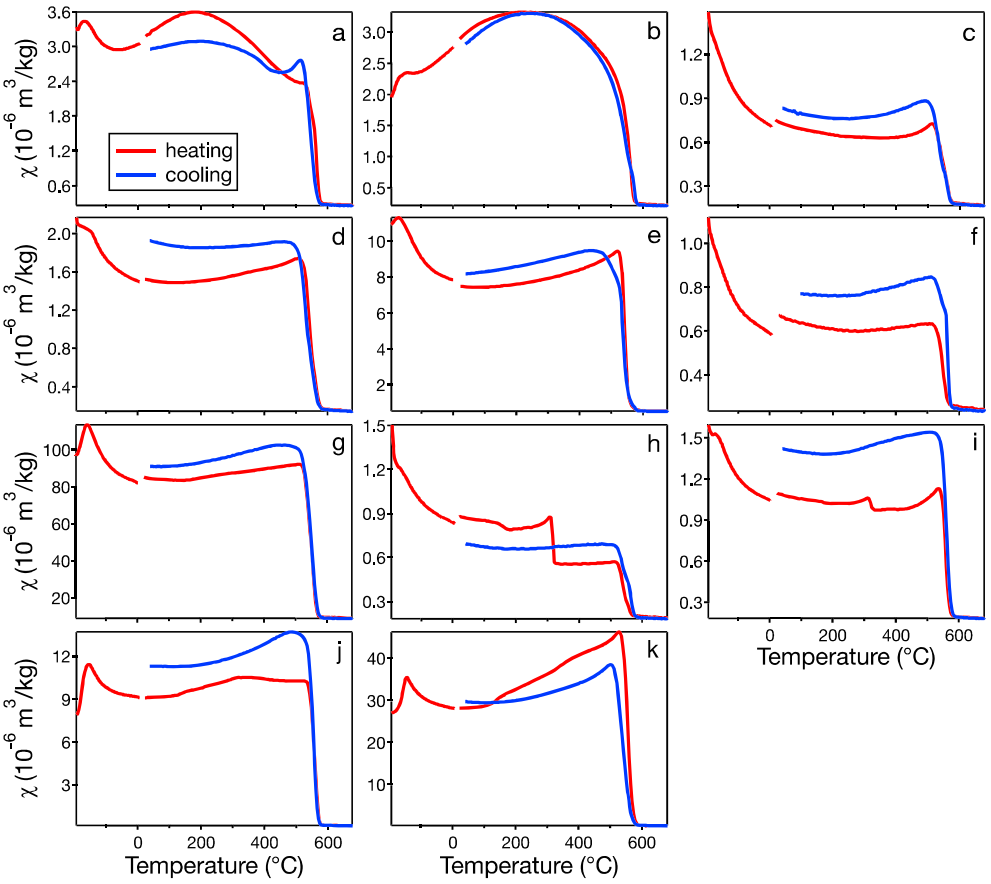

Figure 9. Mass normalized temperature susceptibility curves of representative samples of the (a–c) central series (CS); high density (>3.2 g/cm^3) with (a) high susceptibility, (b) intermediate susceptibility, (c) low susceptibility, (d) upper layered series (ULS), (e) ULS pyroxenite dike, (f) lower layered series (LLS), (g) MZ_gabbro; (h) MZ_gneiss; (i) gabbro; (j) gabbro; and (k) serpentinite. The heating curves are given in red and the cooling curves in blue. All measurements were run in argon.

samples are 550, 539, and 535 °C, respectively. All CS samples contain chrome-spinel, and those with high and intermediate bulk susceptibility contain abundant exsolution of a more iron-rich phase, while those with low bulk susceptibility have little exsolution. The exsolved phase contains variable amounts of Al, Cr, and minor Mg, Ni, and Ti (Pastore, McEnroe, ter Maat, et al., 2018) leading to a range in T_c consistent with the continuous loss of susceptibility from 200 °C to the sharpest decrease at 535–550 °C. The samples with the lowest T_c (by inference, the highest degree of cation substitution) also contain sparser exsolution microstructures and have lower bulk susceptibility compared to those with higher T_c.

The ULS sample, ULS pyroxenite dike, and the LLS show similar temperature susceptibility curves (Figures 9d–9f). The T_c are 539, 540, and 549 °C, respectively. The ULS and ULS pyroxenite dikes show a suppressed Verwey transition, indicating nonstoichiometric or cation-substituted near-end-member magnetite, whereas the LLS lacks a low-temperature transition. The curves are not reversible and have a higher susceptibility after cooling.

The MZ samples have high variability based on whether they formed in contact with the gabbro (Figure 9g) or the garnet gneiss (Figure 9h). The MZ_gabbro sample shows a low-temperature transition at −160 °C (Figure 9g), slightly lower than the Verwey transition literature value of −150 °C and consistent with a small degree of cation substitution (e.g., Moskowitz et al., 1998). The T_c is 551 °C, and the curve is irreversible with a slightly higher susceptibility on cooling. The MZ_gneiss shows a small increase followed by a steep drop in susceptibility at 317 °C (Figure 9h), which is close to the T_c of pyrrhotite, 320 °C (Dekkers, 1989). This feature is not present after heating to 700 °C. A second decrease in susceptibility is present at 540 °C.

The gabbro samples exhibit varying thermomagnetic behavior reflecting the variation in opaque minerals observed in microscopy. The sample containing pyrrhotite, exsolution rods of magnetite from clinopyroxene, and hemo-ilmenite (Figure 9i) shows a decrease in susceptibility at 319 °C, consistent with the presence of magnetic pyrrhotite. A monotonic decrease in susceptibility is observed in this sample 559 °C, suggesting that although both magnetite and hemo-ilmenite may be present these signals cannot be discriminated in this measurement. The gabbro containing only discrete magnetite and exsolution rods of magnetite from clinopyroxene (Figure 9j) has a low-temperature transition at −153 °C and a T_c of 554 °C.

The thermomagnetic curve for serpentinite sample is shown in Figure 9k. There is a sharp Verwey transition at −153 °C, and the sample has a T_c of 574 °C, indicating near-end-member magnetite. The heating curve shows a small enhancement between 300 °C and 440°, which may be indicative of pyrrhotite.

5. Discussion

Identifying the primary magnetic phases in ultramafic rocks, and their properties, is central to understanding magnetic anomalies originating in different parts of the lithosphere. Numerous studies of exposed rocks that originated in the lower crust describe samples that do not reflect their primary magnetic mineralogy, due to later metamorphism, serpentinization, or alteration. Exposures of relatively unaltered ultramafic rocks are uncommon, and the RUC offers a rare opportunity to study deep-crustal rocks with minimal alteration. From the perspective of magnetic anomalies, the timing and P&T conditions of the acquisition of magnetization in the deep crust are important. Below we address these topics and relate the magnetic properties of the RUC to the magnetization of the lower crust and potentially the upper mantle.

5.1. Magnetic Carriers in the RUC

The RUC contains a variety of iron oxides and sulfides, both as discrete grains and as exsolved phases. In the olivine-rich rocks the dominant oxide is a chrome-spinel with exsolution of an iron-rich phase, with compositions approaching end-member magnetite. Clinopyroxene in all formations contains oxide exsolution lamellae of ilmenite, spinel, and magnetite, while orthopyroxene has exsolution lamellae of ilmenite. The dominant sulfides in the RUC are pentlandite, pyrrhotite, pyrite, and chalcopyrite.

Estimated emplacement conditions of the RUC are T of 1450 °C and 6–10 kbar (Bennett et al., 1986; Grant et al., 2016; Larsen et al., 2018). As the intrusion cooled the primary magnetic phases exsolved and acquired their magnetization by cooling through their respective Curie temperatures. Whether these two events were simultaneous or occurred at very different temperatures provides useful information on how the observations in this study can be extrapolated to other geological settings. The geodynamic setting for the RUC is the subject of ongoing research (Larsen et al., 2018).

The dominant oxide phase in the ultramafic formations (CS, ULS, and LLS) is chrome-spinel, which is more abundant in the olivine-rich than the pyroxene-rich rocks. Most chrome-spinel grains contain exsolution blebs, of varying sizes and abundance, of an iron-rich phase, which are distributed throughout the grains (Figures 4a–4c). This microstructure is contrasted with particles that exhibit iron-rich rims surrounding chrome-spinel cores, which has been attributed to metamorphic processes (e.g., Barnes, 2000) but the reaction is not exclusively created by them (e.g., Haggerty, 1976). This rimming is rarely observed in the RUC and is limited to a few drill core samples (Figure 4d) and possibly related to local serpentinization.

The CS samples, in which the Fe-rich exsolution in Cr-spinel is the dominant magnetic phase, show a range a gradual decrease in susceptibility during thermomagnetic measurements from 250 °C to the T_c of ~540 °C during heating. The gradual decrease in susceptibility is interpreted to be due to a range in composition of the Cr-spinel host and Fe-rich exsolution microstructures. This interpretation is in agreement with compositional ranges reported by Pastore, McEnroe, ter Maat, et al. (2018) on dunite samples from the CS, as well as reported progressive changes in T_c in the Fe-Cr spinel solid solution due to compositional variation in the exsolved phase by Francombe (1957) and Robbins et al. (1971). The T_c estimates based on the thermomagnetic curves implies that some exsolution blebs have near-end-member magnetite compositions; however, the partially suppressed Verwey transition also indicates a degree of cation substitution or nonstoichiometry.

Although the chrome-spinel grains crystallized early in the magmatic history, the exsolution of the more iron-rich phase occurred later when the rocks cooled through the solvus temperature of the Cr spinel-

magnetite, at a T slightly below 600 °C. The position of the miscibility gap is indicative of the temperature of exsolution; however, in this system it is a function of both the compositions of the Cr-spinel host and the olivine (Barnes & Roeder, 2001; Sack & Ghiorso, 1991; Ziemniak & Castelli, 2003). Based on the compositions of the olivine in the RUC $Fo_{84.6}$ to $Fo_{76.1}$ (Grant et al., 2016) and of the chrome-spinel (Pastore, McEnroe, ter Maat, et al., 2018), the initial exsolution would have occurred when the rocks cooled to slightly below ~600 to 550 °C, with variations in T dependent on the composition of coexisting olivine (Sack & Ghiorso, 1991). These temperature estimates are consistent with other studies reporting exsolution in chrome-spinel (Colás et al., 2016; Kądziałko-Hofmokl et al., 2008; Muan, 1975; Roeder, 1994) and indicate that the Fe-rich phase formed and acquired their magnetization close to their respective Curie temperatures.

The physical origin of the NRM is likely a combination of multiple processes. Because the solvus temperature is above the T_c of the exsolved phase, it acquires a thermoremanent magnetization (TRM) upon further cooling. Exsolution continues during cooling, and further intergrowths will preserve a thermochemical remanent magnetization (TCRM), because these phases form and acquire a magnetization well below their respective Curie temperatures. The RUC has undergone a complex geodynamic history, which is still unresolved (Larsen et al., 2018). Because the cooling rate of the complex is unknown, we do not specify what portion of the NRM is a TRM or TCRM. There are abundant fine-grained exsolved blebs in the chrome-spinel. We speculate that with prolonged (re-)heating these would have coarsened. Therefore, we infer that the combination of TRM and TCRM should be considered primary.

In addition to these primary components, a secondary viscous or thermoviscous overprint is possible and may even dominate present-day remanence (e.g., Kelso et al., 1993). In Figure 8 on the Day plot (Day et al., 1977) most samples plot close to the SD boundary, and therefore, we consider that thermoviscous processes are more likely than viscous. A contradictory line of evidence comes from the temperature susceptibility data, where measurement show a small or no Hopkinson peak for most samples, which would imply more MD grains (e.g., Clark & Schmidt, 1982; Bina & Henry, 1990), which, in turn, are more susceptible to a viscous overprint. Depending on the cooling history, a thermoviscous or viscous overprint could replace the original TRM/TCRM and at depth the remanent component could be greater than our measurements indicate. Lack of constraint on the tectonic history and uplift rates prohibits us to quantify any of these processes.

Exsolution microstructures are not present in all chrome-spinel grains. Possibly, the intrusion cooled too quickly for unmixing to occur (Evans & Frost, 1975). However, that explanation is unlikely because samples with, and without, exsolution microstructures are located geographically close to each other. More likely the variability in extent of exsolution is due to compositional differences in the chrome-spinel grains and the slight variations in adjacent olivine grains. Another aspect in the exsolved Cr-spinel is whether charge ordering at the interface (Robinson et al., 2006) between the Cr-spinel and exsolution would have an additional magnetic moment.

Most clinopyroxene grains in the RUC contain exsolved lamellae of ilmenite, spinel, and magnetite (Figures 4h and 4i). The T-susceptibility measurements suggest a range of compositions with both near-end-member and cation-substituted magnetite. The Verwey transition commonly observed indicates the presence of near-end-member magnetite (e.g., Figure 9g). In the MZ samples (Figures 9g and 9h), the Curie temperatures of 540 and 551 °C are slightly lower than the T_c of magnetite of 580 °C, which implies a cation substitution of up to ~5–8% (x = 0.05–0.085, 0 <= × <= 1) of the solid solutions $Fe_{3-2x}Cr_{2x}O_4$ for Cr-spinel (Francombe, 1957; Robbins et al., 1971) or $Fe_{3-x}Ti_xO_4$ for titanomagnetite (Bleil & Petersen, 1982). In thin section both discrete magnetite and magnetite lamellae in the clinopyroxene are observed. From these measurements, we cannot determine which is the end-member phase.

The temperature at which the oxide lamellae exsolved from the clinopyroxene is not well constrained. However, using the variation in intersection angles of magnetite lamellae in pyroxene as a function of temperature (Fleet et al., 1980) and exsolution of pyroxene lamellae (Robinson et al., 1971; Robinson et al., 1977), studies of similar microstructures from other localities have consistently reported exsolution temperatures of magnetite in silicates well above the T_c of magnetite (Feinberg et al., 2004; Henry & Medaris, 1980; Savelieva et al., 2016; Sen & Jones, 1988). We conclude that the magnetite lamellae in the clinopyroxene would have acquired a magnetization when cooled through their respective Curie temperatures.

The serpentinized rocks in the RUC contain lizardite (Grannes, 2016), which occurs at temperatures below 400 °C and is considered to have occurred post emplacement. There is a region of pervasive alteration related to the Storvannet fault (Figure 2). These samples commonly contain more than one generation of magnetite, with large composite grains in association with pentlandite and chalcopyrite as well as finer particles in the matrix (Figure 4o). By contrast, other ultramafic samples only show minor alteration, some with serpentinite veins which contain little or no magnetite. Oufi (2002) and Bach et al. (2006) estimated that abundant formation of magnetite only occurs after >75% of peridotite has been serpentinized, which is consistent with the limited secondary magnetite observed in the slightly altered surface samples. In the drill cores, we observed thin local crosscutting serpentinized veins, some related to sulfide-rich fluids, interpreted to be associated with a potential platinum group element deposit (Nikolaisen, 2016).

The oxide mineralogy reported in the Abulangdang intrusion, China (Wang et al., 2014), is dominated by intergrowths of magnetite and ilmenite, and the Cr-spinel is homogeneous and more Ti-rich than the rocks reported here. Cr-spinel found in the Kondyor intrusion (Burg et al., 2009; Pushkarev et al., 2015) is reported in chromitites and formed during serpentinization. In the Chilas mafic-ultramafic complex, Pakistan, the magnetic carriers reported in the ultramafic rocks are similar to those found in this study (Jagoutz et al., 2006; Jagoutz et al., 2007; Jan et al., 1992). The Cr-spinel is considered to have crystallized at high T (>700 °C) and contain a range in abundance of exsolution microstructures, which likely formed during cooling below 600 °C (Jan et al., 1992). The similar results from the RUC and Chilas complex, which both formed at lower crustal levels, may indicate that these rocks are indicative of potential lower crustal magnetic sources.

5.2. Density and Magnetic Properties of Pristine RUC Samples

Identifying what density range is characteristic of the pristine rocks will provide a criterion to examine their magnetic properties. Their properties can then be used to infer the potential contribution to lithospheric magnetization at the surface and in situ. To aid in differentiating the pristine ultramafic rocks from altered, we calculated the theoretical density and the serpentinization degree.

The *minimum* theoretical density calculated from reported compositions of the ultramafic rocks is higher than the *maximum* density measured in the samples. Therefore, the theoretical minimum density is not suitable as a cutoff to define our pristine samples. The overestimation of the calculated density may reflect that Hacker and Abers (2004) estimate rock density solely based on the constituent minerals, and fractures or porosities are not incorporated.

The serpentinization degree calculation from Miller and Christensen (1997) uses a general density of 3.3 g/cm^3 for unserpentinized rocks. Using this calculation, a large number of our samples have a negative, unphysical, serpentinization degree (Figure 6), clearly showing that this assumption does not work. These methods do not yield a reliable way of defining what samples are pristine; therefore, we use a cutoff based on the distribution of the density data on the box plot combined with thin section observations. The bimodal distribution in the CS_surface samples shows a gap in the data around 3.3 g/cm^3, which we use as a cutoff for the CS dunites. For the other ultramafic formations, a cutoff at 3.2 g/cm^3 was used. The samples above these values show little to no alteration (Figures 3a, 3b, 4a, and 4b).

Surprisingly, within the high-density samples there is a clear variability in both susceptibility and NRM values. The ultramafic samples (CS, ULS, and LLS) show a large range in NRM and susceptibility for the high-density samples. Because these samples show little or no evidence of alteration, this variability is attributed to variations in composition, and abundance of the oxides. In addition to variations in the chrome-spinel, the magnetization is strongly controlled by exsolved phases in pyroxenes, which may also vary in abundance and composition.

5.3. Potential Contribution to Crustal Magnetism

Long-wavelength anomalies originate largely within the lithosphere (Purucker & Whaler, 2015; Purucker & Clark, 2011). Here the thickness of the magnetic crust, the part of the lithosphere above the Curie temperature of ferromagnetic minerals, plays an important role. Early studies by Warner and Wasilewski (1995), Wasilewski and Warner (1988), and Wasilewski and Mayhew (1992) report the lithospheric mantle to be too hot and too weakly magnetic to contribute to long-wavelength anomalies. However, more recent studies

propose a potential magnetic contribution from parts of the upper mantle and/or the lower crust (Blakely et al., 2005; Ferré et al., 2013, 2014; Friedman et al., 2014; McEnroe et al., 2018).

To assess the conditions under which rocks with similar magnetic properties to the RUC could (or could not) contribute to lithospheric magnetization, P/T conditions in the lower crust and their consequent effects on magnetic behavior must be considered. Thermal gradients are a key factor in understanding the nature of lithospheric magnetization. Assuming a geothermal gradient of 22 °C/km, the global average for the Earth, the depth to the 550 °C isotherm is ~25 km (Parker, 2014). However, the magnetic crustal thickness depends on factors such as petrology and magnetic mineralogy. Therefore, the magnetic crustal thickness of the continental crust can range between 20 and at least 50 km (Fox Maule et al., 2009), and thermal models indicate that locally the upper part of the mantle can be cooler than the Curie temperature of magnetite, 580 °C (Oleskevich et al., 1999; Thébault et al., 2010).

The use of surface properties for estimations of magnetization deeper in the crust is not without qualification. The effect of pressure on the Curie temperature of magnetite was experimentally determined as 2 .3°C per kb (Gilder & Le Goff, 2008; Schult, 1970). This could lead to an enhancement of the Curie temperature at lower crustal levels of up to 20 °C, resulting in a T_c of magnetite of 600 °C. Dunlop et al. (2010) argue that the magnetization at the surface may be misleading because at elevated temperatures, induced magnetization is enhanced while remanence is simultaneously reduced, particularly for MD grains. Therefore, Dunlop et al. (2010) state that extrapolating Q values at deeper crustal levels from Q values at surface temperatures can be misleading. For SD magnetite, at deep crustal temperatures the Q value close to the blocking temperature is lower than at the surface due to an enhancement of the induced magnetization caused by the Hopkinson peak (Dunlop et al., 1974; Clark & Schmidt, 1982; Dunlop et al., 2010).

The source of a long-wavelength anomaly in the middle or lower crust requires a total magnetization of 1.5–2.5 A/m (Mayhew et al., 1991). When the NRM and induced magnetization (M_i) are in the same direction, that is, the direction of the Earth's field, these vectors sum and result in a positive anomaly. If the NRM and M_i are in opposite directions the anomaly will be reduced. The maximum total magnetization for the ultramafic rocks of the RUC can be calculated by adding the vector-averaged NRM and induced magnetization calculated from susceptibility. For the ultramafic formations (CS, ULS, and LLS), this maximum total magnetization is 2.1 A/m. However, when only considering the pristine ultramafic rocks (density > 3.2 g/cm^3) the maximum total magnetization is 1.4 A/m. The minimum total magnetization, when NRM and M_i are oriented antiparallel, is 0.9 A/m in the direction of remanence for all ultramafic formations, and 0.5 A/m for the pristine samples. The above values are means, therefore a proportion of the samples is stronger, and can be considered as a potential source for long-wavelength anomalies.

Here, we present a data set from ultramafic rocks that range from minor alteration to pristine, which display a range in magnetic properties. The primary magnetic carriers in RUC are exsolved Cr-spinel and magnetite exsolution lamellae in the pyroxenes. Both carriers could contribute to the magnetic signal at lower crustal depths and possibly in the upper part of the mantle when the temperature is lower than the T_c of magnetite. The ultramafic cumulates of the RUC are a magmatic conduit system, which intruded at depths of 25–35 km at pressures of 6–8 kb (Larsen et al., 2018). The volume of rocks is of crucial importance for a potential source of long-wavelength anomalies, and due to the volume of the rocks of the RUC, similar rocks are good candidates as a source of magnetic anomalies deep in the crust, or in the upper mantle, given the temperature is below the T_c of magnetite and contain the same exsolution microstructures.

6. Conclusions

We presented the petrophysical properties of unusually pristine ultramafic rocks of the RUC. The RUC formed as a deep-seated magmatic conduit system and consists of ultramafic cumulates. The primary sources of magnetization in the ultramafic rocks are the exsolution microstructures in the chrome-spinel and magnetite lamellae in the clinopyroxene. The Fe-rich phase exsolved at a T close to its Curie temperature. The oxide exsolution lamellae from clinopyroxene formed at higher temperatures and later oxy-exsolved to magnetite and ilmenite.

Further, we identified the properties of the ultramafic rocks by petrographic characterization and by density measurements. The high-density, pristine ultramafic samples show a large range in both NRM and

susceptibility values, which are correlated to the size and abundance of the different magnetic oxides and microstructures therein. The primary magnetic carriers are stable at temperatures up to the Curie temperature of magnetite. We consider these phases to be source of magnetization in the lower crust or uppermost mantle, with the effects of pressure possibly stable up to 600 °C. Rocks similar to the RUC may be a source of LWA if they contain the primary mineralogy as we found in this study.

Acknowledgments
This research was supported by NTNU and a Norwegian Research Council grant (222666 to S. M.). Some magnetic measurements were made during a visiting fellowship to the IRM, which is supported by an NSF instruments and facilities grants. Nordic mining is acknowledged for access to sample the RUC deep drill cores. Alex Michels, Zeudia Pastore, and Alexandra McEnroe are thanked for their help with magnetic measurements and Zeudia Pastore for her assistance in Geosoft. We thank two anonymous reviewers for constructive review comments. The measured petrophysical properties and hysteresis ratios of the samples can be found in Table S1 and a plot of susceptibility versus density of each of the ultramafic formations in Figure S1.

References

Andréasson, P.-G., Svenningsen, O. M., & Albrecht, L. (1998). Dawn of Phanerozoic orogeny in the North Atlantic tract; evidence from the seve-kalak superterrane, scandinavian caledonides. *GFF*, *120*(2), 159–172. https://doi.org/10.1080/11035899801202159

Bach, W., Paulick, H., Garrido, C. J., Ildefonse, B., Meurer, W. P., & Humphris, S. E. (2006). Unraveling the sequence of serpentinization reactions: Petrography, mineral chemistry, and petrophysics of serpentinites from MAR 15°N (ODP Leg 209, Site 1274). *Geophysical Research Letters*, *33*, L13306. https://doi.org/10.1029/2006GL025681

Barnes, S.-J. (2000). Chromite in komatiites, II. Modification during greenschist to mid-amphibolite facies metamorphism. *Journal of Petrology*, *41*(3), 387–409. https://doi.org/10.1093/petrology/41.3.387

Barnes, S.-J., & Roeder, P. L. (2001). The range of spinel compositions in terrestrial mafic and ultramafic rocks. *Journal of Petrology*, *42*(12), 2279–2302. https://doi.org/10.1093/petrology/42.12.2279

Bennett, C. M. (1972). *Report to accompany the geological map of the Reinfjord ultramafic complex* (pp. 1–14). Reinfjord, N Troms: Norges Geologiske Undersokelse.

Bennett, M. C. (1974). The emplacement of a high temperature peridotite in the seiland province of the Norwegian Caledonides. *Journal of the Geological Society*, *130*(3), 205–226. https://doi.org/10.1144/gsjgs.130.3.0205

Bennett, M. C., Emblin, S. R., Robins, B., & Yeo, W. J. A. (1986). High-temperature ultramafic complexes in the North Norwegian Caledonides: I—Regional setting and field relationships. *Norges Geologiske Undersokelse*, *405*, 1–40.

Bina, M. M., & Henry, B. (1990). Magnetic-properties, opaque mineralogy and magnetic anisotropies of serpentinized peridotites from Odp Hole 670a Near the Mid-Atlantic Ridge. *Physics of the Earth and Planetary Interiors*, *65*(1–2), 88–103. https://doi.org/10.1016/0031-9201(90)90078-C

Blakely, R. J., Brocher, T. M., & Wells, R. E. (2005). Subduction-zone magnetic anomalies and implications for hydrated forearc mantle. *Geology*, *33*(6), 445–444. https://doi.org/10.1130/G21447.1

Bleil, U., & Petersen, N. (1982). Magnetic properties of natural minerals. In G. Angenheister (Ed.), *Numerical data and functional relationships in science and technology, Group V: Geophysics and Space Research* (pp. 308–365). New York: Springer.

Bostock, M. G., Hyndman, R. D., Rondenay, S., & Peacock, S. M. (2002). An inverted continental Moho and serpentinization of the forearc mantle. *Nature*, *417*(6888), 536–538. https://doi.org/10.1038/417536a

Brown, L. L., & McEnroe, S. A. (2008). Magnetic properties of anorthosites: A forgotten source for planetary magnetic anomalies? *Geophysical Research Letters*, *35*, E10003. https://doi.org/10.1029/2007GL032522

Burg, J.-P., Bodinier, J. L., Gerya, T., Bedini, R. M., Boudier, F., Dautria, J. M., et al. (2009). Translithospheric mantle Diapirism: Geological evidence and numerical modelling of the Kondyor zoned ultramafic complex (Russian Far-East). *Journal of Petrology*, *50*(2), 289–321. https://doi.org/10.1093/petrology/egn083

Carporzen, L., Gilder, S. A., & Hart, R. J. (2006). Origin and implications of two Verwey transitions in the basement rocks of the Vredefort meteorite crater, South Africa. *Earth and Planetary Science Letters*, *251*(3-4), 305–317. https://doi.org/10.1016/j.epsl.2006.09.013

Clark, D. A. (2014). Methods for determining remanent and total magnetisations of magnetic sources – A review. *Exploration Geophysics*, *45*(4), 271–304. https://doi.org/10.1071/EG14013

Clark, D. A., & Schmidt, P. W. (1982). Theoretical-analysis of thermomagnetic properties, low-temperature hysteresis and domain-structure of titanomagnetites. *Physics of the Earth and Planetary Interiors*, *30*(4), 300–316. https://doi.org/10.1016/0031-9201(82)90029-2

Colás, V., Padrón-Navarta, J. A., González-Jiménez, J. M., Griffin, W. L., Fanlo, I., Oreilly, S. Y., et al. (2016). Compositional effects on the solubility of minor and trace elements in oxide spinel minerals: Insights from crystal-crystal partition coefficients in chromite exsolution. *American Mineralogist*, *101*(6), 1360–1372. https://doi.org/10.2138/am-2016-5611

Corfu, F., Roberts, R. J., Torsvik, T. H., Ashwal, L. D., & Ramsay, D. M. (2007). Peri-Gondwanan elements in the Caledonian Nappes of Finnmark, northern Norway: Implications for the paleogeographic framework of the Scandinavian Caledonides. *American Journal of Science*, *307*(2), 434–458. https://doi.org/10.2475/02.2007.05

Day, R., Fuller, M., & Schmidt, V. A. (1977). Hysteresis properties of titanomagnetites: Grain-size and compositional dependence. *Physics of the Earth and Planetary Interiors*, *13*(4), 260–267. https://doi.org/10.1016/0031-9201(77)90108-X

Dekkers, M. J. (1989). Magnetic properties of natural pyrrhotite. II. High- and low-temperature behaviour of Jrs and TRM as function of grain size. *Physics of the Earth and Planetary Interiors*, *57*(3-4), 266–283. https://doi.org/10.1016/0031-9201(89)90116-7

Dunlop, D. J. (2002). Theory and application of the Day plot (Mrs/MsversusHcr/Hc) 1. Theoretical curves and tests using titanomagnetite data. *Journal of Geophysical Research*, *107*(B3), 2056. https://doi.org/10.1029/2001JB000486

Dunlop, D. J., Özdemir, Ö., & Costanzo-Alvarez, V. (2010). Magnetic properties of rocks of the Kapuskasing uplift (Ontario, Canada) and origin of long-wavelength magnetic anomalies. *Geophysical Journal International*, *183*(2), 645–658. https://doi.org/10.1111/j.1365-246X.2010.04778.x

Dunlop, D. J., Stacey, F. D., & Gillingham, D. E. W. (1974). The origin of thermoremanent magnetization: Contribution of pseudo-single-domain magnetic moments. *Earth and Planetary Science Letters*, *21*(3), 288–294. https://doi.org/10.1016/0012-821X(74)90163-0

Eales, H. V., Wilson, A. H., & Reynolds, I. M. (1988). Complex unmixed spinels in layered intrusions within an obducted ophiolite in the Natal-Namaqua Mobile Belt. *Mineralium Deposita*, *23*(2), 150–157. https://doi.org/10.1007/BF00206665

Emblin, S. R. (1985). The Reinfjord ultramafic complex, Seiland province: Emplacement history and magma chamber model. (PhD thesis). University of Bristol, UK.

Evans, B. W., & Frost, B. R. (1975). Chrome-spinel in progressive metamorphism - preliminary analysis. *Geochimica et Cosmochimica Acta*, *39*(6–7), 959–972. https://doi.org/10.1016/0016-7037(75)90041-1

Facer, J., Downes, H., & Beard, A. (2009). In situ serpentinization and hydrous fluid metasomatism in spinel Dunite xenoliths from the Bearpaw Mountains, Montana, USA. *Journal of Petrology*, *50*(8), 1443–1475. https://doi.org/10.1093/petrology/egp037

Feinberg, J. M., Wenk, H.-R., Renne, P. R., & Scott, G. R. (2004). Epitaxial relationships of clinopyroxene-hosted magnetite determined using electron backscatter diffraction (EBSD) technique. *American Mineralogist*, *89*(2–3), 462–466. https://doi.org/10.2138/am-2004-2-328

Ferré, E. C., Friedman, S. A., Martín-Hernández, F., Feinberg, J. M., Conder, J. A., & Ionov, D. A. (2013). The magnetism of mantle xenoliths and potential implications for sub-Moho magnetic sources. *Geophysical Research Letters*, *40*, 105–110. https://doi.org/10.1029/2012GL054100

Ferré, E. C., Friedman, S. A., Martín-Hernández, F., Feinberg, J. M., Till, J. L., Ionov, D. A., & Conder, J. A. (2014). Eight good reasons why the uppermost mantle could be magnetic. *Tectonophysics*, *624-625*, 3–14. https://doi.org/10.1016/j.tecto.2014.01.004

Finlay, C. C., Maus, S., Beggan, C. D., Bondar, T. N., Chambodut, A., Chernova, T. A., et al. (2010). International Geomagnetic Reference Field: the eleventh generation. *Geophysical Journal International*, *183*(3), 1216–1230. https://doi.org/10.1111/j.1365-246X.2010.04804.x

Fleet, M. E., Bilcox, G. A., & Barnett, R. L. (1980). Oriented magnetite inclusions in pyroxenes from the Grenville province. The Canadian Mineralogist, 1–11.

Fox Maule, C., Purucker, M. E., & Olsen, N. (2009). Inferring magnetic crustal thickness and geothermal heat flux from crustal magnetic field models. Estimating the geothermal heat flux beneath the Greenland ice sheet. *Danish Climate Centre Report*, *9*(09).

Francombe, M. H. (1957). Lattice changes in spinel-type iron chromites. *Journal of Physics and Chemistry of Solids*, *3*(1–2), 37–43. https://doi.org/10.1016/0022-3697(57)90045-8

Friedman, S. A., Feinberg, J. M., Ferré, E. C., Demory, F., Martín-Hernández, F., Conder, J. A., & Rochette, P. (2014). Craton vs. rift uppermost mantle contributions to magnetic anomalies in the United States interior. *Tectonophysics*, *624-625*, 15–23. https://doi.org/10.1016/j.tecto.2014.04.023

Frost, B. R., & Shive, P. N. (1986). Magnetic mineralogy of the lower continental-crust. *Journal of Geophysical Research*, *91*(B6), 6513–6521. https://doi.org/10.1029/JB091iB06p06513

Gee, D. G., Ladenberger, A., Dahlqvist, P., Majka, J., Be'eri-Shlevin, Y., Frei, D., & Thomsen, T. (2014). The Baltoscandian margin detrital zircon signatures of the central Scandes. *Geological Society, London, Special Publications*, *390*(1), 131–155. https://doi.org/10.1144/SP390.20

Gilder, S. A., & Le Goff, M. (2008). Systematic pressure enhancement of titanomagnetite magnetization. *Geophysical Research Letters*, *35*, B06104. https://doi.org/10.1029/2008GL033325

Grannes, K. R. (2016). Cryptic variations of olivene and clinopyroxene in the RF-4 drill-core: A geochemical study of the Reinfjord Ultramafic Complex, Norway. (MSc thesis). Norwegian University of Science and Technology.

Grant, T. B., Larsen, R. B., Anker-Rasch, L., Grannes, K. R., Iljina, M., McEnroe, S., et al. (2016). Anatomy of a deep crustal volcanic conduit system: The Reinfjord Ultramafic Complex, Seiland Igneous Province, Northern Norway. *Lithos*, *252-253*(C), 200–215. https://doi.org/10.1016/j.lithos.2016.02.020

Griffin, W. L., Sturt, B. A., O'Neill, C. J., Kirkland, C. L., & O'Reilly, S. Y. (2013). Intrusion and contamination of high-temperature dunitic magma: The Nordre Bumandsfjord pluton, Seiland, Arctic Norway. *Contributions to Mineralogy and Petrology*, *165*(5), 903–930. https://doi.org/10.1007/s00410-012-0841-6

Hacker, B. R., & Abers, G. A. (2004). Subduction Factory 3: An Excel worksheet and macro for calculating the densities, seismic wave speeds, and H_2O contents of minerals and rocks at pressure and temperature. *Geochemistry, Geophysics, Geosystems*, *5*, Q01005. https://doi.org/10.1029/2003GC000614

Haggerty, S. E. (1976). Chapter 8. Opaque mineral oxides in terrestrial igneous rocks. In D. Rumble (Ed.), *Oxide Minerals* (pp. 303–502). Berlin, Boston: De Gruyter. https://doi.org/10.1515/9781501508561-013

Heilbronner, R., & Barret, S. (Eds) (2014). *Image Analysis in Earth Sciences*. Berlin: Springer-Verlag. https://doi.org/10.1007/978-3-642-10343-8

Henry, D. J., & Medaris, L. (1980). Application of pyroxene and olivine-spinel geothermometers to spinel peridotites in southwestern Oregon. *American Journal of Science*, *280*, 211–231.

Hyndman, R. D., & Peacock, S. M. (2003). Serpentinization of the forearc mantle. *Earth and Planetary Science Letters*, *212*(3–4), 417–432. https://doi.org/10.1016/S0012-821X(03)00263-2

Idárraga-García, J., & Vargas, C. A. (2018). Depth to the bottom of magnetic layer in South America and its relationship to Curie isotherm, Moho depth and seismicity behavior. *Geodesy and Geodynamics*, *9*(1), 93–107. https://doi.org/10.1016/j.geog.2017.09.006

Iljina, M., 2012. Reinfjord drilling and mapping campaigns in 2012: Geochemical observations, Discussion of ore genesis and exploration implications. *Report. Nordic Mining ASA* (26 pp.).

Jagoutz, O., Müntener, O., Burg, J., Ulmer, P., & Jagoutz, E. (2006). Lower continental crust formation through focused flow in km-scale melt conduits: The zoned ultramafic bodies of the Chilas Complex in the Kohistan island arc (NW Pakistan). *Earth and Planetary Science Letters*, *242*(3–4), 320–342. https://doi.org/10.1016/j.epsl.2005.12.005

Jagoutz, O., Müntener, O., Ulmer, P., Pettke, T., Burg, J. P., Dawood, H., & Hussain, S. (2007). Petrology and mineral chemistry of lower crustal intrusions: The Chilas Complex, Kohistan (NW Pakistan). *Journal of Petrology*, *48*(10), 1895–1953. https://doi.org/10.1093/petrology/egm044

Jan, M. Q., Khan, M. A., & Windley, B. F. (1992). Exsolution in Al-Cr-Fe3+—rich spinels from the Chilas mafic- ultramafic complex, Pakistan. *American Mineralogist*, *77*(9–10), 1074–1079.

Johnson, D. (2011). *Quality assessment and interpretation report on the Reinfjord and Lokkarfjord SkyTEM surveys*. Vancouver, Canada: Revelation Geoscience Ltd.

Kądziałko-Hofmokl, M., Delura, K., Bylina, P., Jeleńska, M., & Kruczyk, J. (2008). Mineralogy and magnetism of Fe-Cr spinel series minerals from podiform chromitites and dunites from Tąpadła (Sudetic ophiolite, SW Poland) and their relationship to palaeomagnetic results of the dunites. *Geophysical Journal International*, *175*(3), 885–900. https://doi.org/10.1111/j.1365-246X.2008.03933.x

Kakol, Z., Sabol, J., Stickler, J., & Honig, J. M. (1992). Effect of low-level titanium (iv) doping on the resistivity of magnetite near the Verwey transition. *Physical Review B*, *46*(4), 1975–1978. https://doi.org/10.1103/PhysRevB.46.1975

Kasama, T., McEnroe, S. A., Ozaki, N., Kogure, T., & Putnis, A. (2004). Effects of nanoscale exsolution in hematite–ilmenite on the acquisition of stable natural remanent magnetization. *Earth and Planetary Science Letters*, *224*(3–4), 461–475. https://doi.org/10.1016/j.epsl.2004.05.027

Kelso, P. R., Banerjee, S. K., & Teyssier, C. (1993). Rock magnetic-properties of the Arunta Block, Central-Australia, and their implication for the interpretation of long-wavelength magnetic-anomalies. *Journal of Geophysical Research-Solid Earth and Planets*, *98*(B9), 15,987–15,999. https://doi.org/10.1029/93JB01158

Kiss, J., Szarka, L., & Prácser, E. (2005). Second-order magnetic phase transition in the Earth. *Geophysical Research Letters*, *32*, L24310. https://doi.org/10.1029/2005GL024199

Klein, F., Bach, W., Humphris, S. E., Kahl, W. A., Jons, N., Moskowitz, B., & Berquo, T. S. (2014). Magnetite in seafloor serpentinite—Some like it hot. *Geology*, *42*(2), 135–138. https://doi.org/10.1130/G35068.1

Klein, F., Bach, W., Jöns, N., McCollom, T., Moskowitz, B., & Berquó, T. (2009). Iron partitioning and hydrogen generation during serpentinization of abyssal peridotites from 15°N on the Mid-Atlantic Ridge. *Geochimica et Cosmochimica Acta*, *73*(22), 6868–6893. https://doi.org/10.1016/j.gca.2009.08.021

Kletetschka, G., & Stout, J. H. (1998). The origin of magnetic anomalies in lower crustal rocks, Labrador. *Geophysical Research Letters*, *25*(2), 199–202. https://doi.org/10.1029/97GL03506

Larsen, R. B., Grant, T., Sørensen, B. E., Tegner, C., McEnroe, S., Pastore, Z., et al. (2018). Portrait of a giant deep-seated magmatic conduit system: The Seiland Igneous Province. *Lithos*, *296-299*(C), 600–622. https://doi.org/10.1016/j.lithos.2017.11.013

Li, Z., Zheng, J., Zeng, Q., Liu, Q., & Griffin, W. L. (2014). Magnetic mineralogy of pyroxenite xenoliths from Hannuoba basalts, northern North China Craton: Implications for magnetism in the continental lower crust. *Journal of Geophysical Research: Solid Earth*, *119*, 806–821. https://doi.org/10.1002/2013JB010599

Lillis, R. J., Purucker, M. E., Halekas, J. S., Louzada, K. L., Stewart-Mukhopadhyay, S. T., Manga, M., & Frey, H. V. (2010). Study of impact demagnetization at Mars using Monte Carlo modeling and multiple altitude data. *Journal of Geophysical Research*, *115*, 790–722. http://doi.org/10.1029/2009JE003556

Liu, Q., Wang, H., Zheng, J., Zeng, Q., & Liu, Q. (2013). Petromagnetic properties of granulite-facies rocks from the northern North China Craton: Implications for magnetic and evolution of the continental lower crust. *Journal of Earth Science*, *24*(1), 12–28. https://doi.org/10.1007/s12583-013-0314-5

Loferski, P. J., & Lipin, B. R. (1983). Exsolution in metamorphosed chromite from the Red-Lodge District, Montana. *American Mineralogist*, *68*(7–8), 777–789.

Maffione, M., Morris, A., Plümper, O., & van Hinsbergen, D. J. J. (2014). Magnetic properties of variably serpentinized peridotites and their implication for the evolution of oceanic core complexes. *Geochemistry, Geophysics, Geosystems*, *15*, 923–944. https://doi.org/10.1002/2013GC004993

Martín-Hernández, F., Ferré, E. C., & Friedman, S. A. (2014). Remanent magnetization in fresh xenoliths derived from combined demagnetization experiments: Magnetic mineralogy, origin and implications for mantle sources of magnetic anomalies. *Tectonophysics*, *624-625*, 24–31. https://doi.org/10.1016/j.tecto.2014.04.006

Mayhew, M. A., Wasilewski, P. J., & Johnson, B. D. (1991). Crustal magnetization and temperature at depth beneath the Yilgarn Block, Western-Australia inferred from Magsat data. *Earth and Planetary Science Letters*, *107*(3–4), 515–522. https://doi.org/10.1016/0012-821X(91)90097-2

McCammon, C. A., McEnroe, S. A., Robinson, P., Fabian, K., & Burton, B. P. (2009). High efficiency of natural lamellar remanent magnetisation in single grains of ilmeno-hematite calculated using Mössbauer spectroscopy. *Earth and Planetary Science Letters*, *288*(1–2), 268–278. https://doi.org/10.1016/j.epsl.2009.09.030

McEnroe, S. A., & Brown, L. L. (2000). A closer look at remanence-dominated aeromagnetic anomalies: Rock magnetic properties and magnetic mineralogy of the Russell Belt microcline-sillimanite gneiss, northwest Adirondack Mountains, New York. *Journal of Geophysical Research*, *105*(B7), 16,437–16,456. https://doi.org/10.1029/2000JB900051

McEnroe, S. A., Brown, L. L., & Robinson, P. (2009). Remanent and induced magnetic anomalies over a layered intrusion: Effects from crystal fractionation and magma recharge. *Tectonophysics*, *478*(1–2), 119–134. https://doi.org/10.1016/j.tecto.2008.11.021

McEnroe, S. A., Harrison, R., Robinson, P., Golla, U., & Jercinovic, M. J. (2001a). The effect of fine-scale microstructures in titanohematite on the acquisition and stability of natural remanent magnetization in granulite facies metamorphic rocks from southwest Sweden: Implications for crustal magnetism. *Journal of Geophysical Research*, *106*(B12), 30,523–30,546. https://doi.org/10.1029/2001JB000180

McEnroe, S. A., Harrison, R. J., Robinson, P., & Langenhorst, F. (2002). Nanoscale haematite-ilmenite lamellae in massive ilmenite rock: An example of "lamellar magnetism" with implications for planetary magnetic anomalies. *Geophysical Journal International*, *151*(3), 890–912. https://doi.org/10.1046/j.1365-246X.2002.01813.x

McEnroe, S. A., Harrison, R. J., Robinson, P., Golla, U., & Jercinovic, M. J. (2001b). Effect of fine-scale microstructures in titanohematite on the acquisition and stability of natural remanent magnetization in granulite facies metamorphic rocks, Southwest Sweden: Implications for crustal magnetism. *Journal of Geophysical Research*, *106*(B12), 30,523–30,546. https://doi.org/10.1029/2001JB000180

McEnroe, S. A., Langenhorst, F., Robinson, P., Bromiley, G. D., & Shaw, C. S. J. (2004). What is magnetic in the lower crust? *Earth and Planetary Science Letters*, *226*(1–2), 175–192. https://doi.org/10.1016/j.epsl.2004.07.020

McEnroe, S. A., Robinson, P., Church, N. S., & Purucker, M. E. (2018). Magnetism at depth: A view from an ancient continental subduction and collision zone. *Geochemistry, Geophysics, Geosystems*, *279*, 936–925. https://doi.org/10.1002/2017GC007344

McEnroe, S. A., Robinson, P., Langenhorst, F., Frandsen, C., Terry, M. P., & Boffa Ballaran, T. (2007). Magnetization of exsolution intergrowths of hematite and ilmenite: Mineral chemistry, phase relations, and magnetic properties of hemo-ilmenite ores with micron- to nanometer-scale lamellae from Allard Lake, Quebec. *Journal of Geophysical Research*, *112*, B10103. https://doi.org/10.1029/2007JB004973

McEnroe, S. A., Robinson, P., Miyajima, N., Fabian, K., Dyar, D., & Sklute, E. (2016). Lamellar magnetism and exchange bias in billion-year-old titanohematite with nanoscale ilmenite exsolution lamellae: I. Mineral and magnetic characterization. *Geophysical Journal International*, *206*(1), 470–486. https://doi.org/10.1093/gji/ggw155

McEnroe, S. A., Robinson, P., & Panish, P. T. (2001c). Aeromagnetic anomalies, magnetic petrology, and rock magnetism of hemo-ilmenite- and magnetite-rich cumulate rocks from the Sokndal Region, South Rogaland, Norway. *American Mineralogist*, *86*(11-12), 1447–1468. https://doi.org/10.2138/am-2001-11-1213

Michels, A. C., McEnroe, S. A., & Fichler, C. (2018). Geophysical expression of the Leka Ophiolite, Norway, modeled from integrated gravity, magnetic and petrophysical data. *Norwegian Journal of Geology*, 1–24. https://doi.org/10.17850/njg98-1-07

Miller, D. J., & Christensen, N. I. (1997). Seismic velocities of lower crustal and upper mantle rocks from the slow-spreading Mid-Atlantic Ridge, south of the Kane Transform Zone (MARK). *Proceedings of the Ocean Drilling Program, 153 Scientific Results*, *153*. https://doi.org/10.2973/odp.proc.sr.153.043.1997

Moskowitz, B. M., Jackson, M. J., & Kissel, C. (1998). Low-temperature magnetic behavior of titanomagnetites. *Earth and Planetary Science Letters*, *157*(3), 141–149. https://doi.org/10.1016/S0012-821X(98)00033-8

Muan, A. (1975). Phase relations in chromium oxide-containing systems at elevated-temperatures. *Geochimica et Cosmochimica Acta*, *39*(6–7), 781–802. https://doi.org/10.1016/0016-7037(75)90025-3

Nikolaisen, E. (2016). Platinum group elements in the Reinfjord Ultramafic Complex (MSc Thesis). Norwegian University of Science and Technology.

Oleskevich, D. A., Hyndman, R. D., & Wang, K. (1999). The updip and downdip limits to great subduction earthquakes: Thermal and structural models of Cascadia, south Alaska, SW Japan, and Chile. *Journal of Geophysical Research*, *104*(B7), 14,965–14,991. https://doi.org/10.1029/1999JB900060

Oosterom, M. G. (1954). En hornblenderik sone i Seiland-peridotitten. *Norges Geologiske Undersokelse Bulletin*, *188*, 51–53.
Oufi, O. (2002). Magnetic properties of variably serpentinized abyssal peridotites. *Journal of Geophysical Research*, *107*(B5), 2095. https://doi.org/10.1029/2001JB000549
Parker, E. H. Jr. (2014). Crustal magnetism, tectonic inheritance, and continental rifting in the southeastern United States. *GSA Today*, *24*(4), 4–9. https://doi.org/10.1130/GSAT-G192A.1
Pastore, Z. (2018). Geophysical mapping of the mafic and ultramafic rocks of the Seiland Igneous Province from the kilometer to the micrometer scale (PhD thesis). Norwegian University of Science and Technology, Trondheim, Norway
Pastore, Z., Fichler, C., & McEnroe, S. A. (2016). The deep crustal structure of the mafic–ultramafic Seiland Igneous Province of Norway from 3-D gravity modelling and geological implications. *Geophysical Journal International*, *207*(3), 1653–1666. https://doi.org/10.1093/gji/ggw362
Pastore, Z., Fichler, C., & McEnroe, S. A. (2018). Magnetic anomalies of the mafic/ultramafic Seiland Igneous Province. *Norwegian Journal of Geology*, 1–23. https://doi.org/10.17850/njg98-1-06
Pastore, Z., McEnroe, S. A., ter Maat, G. W., Oda, H., Church, N. S., & Fumagalli, P. (2018). Mapping magnetic sources at the millimeter to micrometer scale in dunite and serpentinite by high-resolution magnetic microscopy. *Lithos*, *323*, 174–190. https://doi.org/10.1016/j.lithos.2018.09.018
Paterson, G. A., Zhao, X., Jackson, M., & Heslop, D. (2018). Measuring, processing, and analyzing Hysteresis Data. *Geochemistry, Geophysics, Geosystems*, *19*, 1925–1945. https://doi.org/10.1029/2018GC007620
Pilkington, M., & Percival, J. A. (1999). Crustal magnetization and long-wavelength aeromagnetic anomalies of the Minto block, Quebec. *Journal of Geophysical Research*, *104*, 7513–7526. https://doi.org/10.1029/1998JB900121
Purucker, M. E., & Clark, D. A. (2011). Mapping and interpretation of the lithospheric magnetic field. In *Geomagnetic observations and models* (pp. 311–337). Dordrecht: Springer, Dordrecht. https://doi.org/10.1007/978-90-481-9858-0_13
Purucker, M. E., & Whaler, K. A. (2015). Crustal magnetism. In *Treatise on geophysics* (pp. 185–218). Elsevier. https://doi.org/10.1016/B978-0-444-53802-4.00100-7
Pushkarev, E. V., Kamenetsky, V. S., Morozova, A. V., Khiller, V. V., Glavatskykh, S. P., & Rodemann, T. (2015). Ontogeny of ore Cr-spinel and composition of inclusions as indicators of the pneumatolytic–hydrothermal origin of PGM-bearing chromitites from Kondyor massif, the Aldan Shield. *Geology of Ore Deposits*, *57*(5), 352–380. https://doi.org/10.1134/S1075701515050049
Ramdohr, P. (1980). *The ore minerals and their intergrowths*. Oxford, UK: Pergamon.
Ravat, D., Whaler, K. A., Pilkington, M., Sabaka, T., & Purucker, M. (2002). Compatibility of high-altitude aeromagnetic and satellite-altitude magnetic anomalies over Canada. *Geophysics*, *67*(2), 546–554. https://doi.org/10.1190/1.1468615
Robbins, M., Wertheim, G. K., Sherwood, R. C., & Buchanan, D. N. E. (1971). Magnetic properties and site distributions in the system FeCr2O4-Fe3O4Fe2 Cr2—xFex3 O4. *Journal of Physics and Chemistry of Solids*, *32*(3), 717–729. https://doi.org/10.1016/S0022-3697(71)80412-2
Roberts, A. P., Heslop, D., Zhao, X., & Pike, C. R. (2014). Understanding fine magnetic particle systems through use of first-order reversal curve diagrams. *Reviews of Geophysics*, *52*, 557–602. https://doi.org/10.1002/2014RG000462
Roberts, A. P., Tauxe, L., Heslop, D., Zhao, X., & Jiang, Z. (2018). A critical appraisal of the "Day" diagram. *Journal of Geophysical Research: Solid Earth*, *123*, 2618–2644. https://doi.org/10.1002/2017JB015247
Roberts, D. (1985). The Caledonian fold belt in Finnmark: A synopsis. *Norges Geologiske Undersokelse Bulletin*, *403*, 161–177.
Roberts, R. J. (2007). The Seiland Igneous Province, Northern Norway: Age, provenance, and tectonic significance Richard James Roberts. PhD Thesis, 1–241.
Roberts, R. J., Corfu, F., Torsvik, T. H., Ashwal, L. D., & Ramsay, D. M. (2006). Short-lived mafic magmatism at 560–570 Ma in the northern Norwegian Caledonides: U–Pb zircon ages from the Seiland Igneous Province. *Geological Magazine*, *143*(06), 887–817. https://doi.org/10.1017/S0016756806002512
Robins, B., & Gardner, P. M. (1975). The magmatic evolution of the Seiland province, and Caledonian plate boundaries in northern Norway. *Earth and Planetary Science Letters*, *26*(2), 167–178. https://doi.org/10.1016/0012-821X(75)90084-9
Robinson, P., Harrison, R. J., & McEnroe, S. A. (2006). Fe2+/Fe3+ charge ordering in contact layers of lamellar magnetism: Bond valence arguments. *American Mineralogist*, *91*(1), 67–72. https://doi.org/10.2138/am.2006.2012
Robinson, P., Jaffe, H. W., Ross, M., & Klein, C. (1971). Orientation of exsolution lamellae in clinopyroxenes and clinoamphiboles—Consideration of optimal phase boundaries. *American Mineralogist*, *56*(5-6), 909–939.
Robinson, P., McEnroe, S. A., Miyajima, N., Fabian, K., & Church, N. (2016). Remanent magnetization, magnetic coupling, and interface ionic configurations of intergrown rhombohedral and cubic Fe-Ti oxides: A short survey. *American Mineralogist*, *101*(3), 518–530. https://doi.org/10.2138/am-2016-5519
Robinson, P., Ross, M., Nord, G. L., Smyth, J. R., & Jaffe, H. W. (1977). Exsolution lamellae in augite and pigeonite—Fossil indicators of lattice-parameters at high-temperature and pressure. *American Mineralogist*, *62*(9–10), 857–873.
Roeder, P. L. (1994). Chromite; from the fiery rain of chondrules to the Kilauea Iki lava lake. *The Canadian Mineralogist*, *32*(4), 729–746.
Sack, R. O., & Ghiorso, M. S. (1991). Chromian spinels as petrogenetic indicators; thermodynamics and petrological applications. *American Mineralogist*, *76*(5-6), 827–847.
Savelieva, G. N., Batanova, V. G., & Sobolev, A. V. (2016). Pyroxene–Cr-spinel exsolution in mantle lherzolites of the Syum-Keu ophiolite massif (Arctic Urals). *Russian Geology and Geophysics*, *57*(10), 1419–1436. https://doi.org/10.1016/j.rgg.2015.12.001
Schanche, M., Iljina, M., & Larsen, R. (2012). New nickel, copper and platinum-group element discoveries in northern Norway. Mineralproduksjon, 91–99.
Schlinger, C. M. (1985). Magnetization of lower crust and interpretation of regional magnetic anomalies: Example from Lofoten and Vesterålen, Norway. *Journal of Geophysical Research*, *90*, 11484. https://doi.org/10.1029/jb090ib13p11484
Schult, A. (1970). Effect of pressure on the Curie temperature of titanomagnetites [(1 — x) ·Fe3O4 — x ·TiFe2O4]. *Earth and Planetary Science Letters*, *10*(1), 81–86. https://doi.org/10.1016/0012-821X(70)90067-1
Sen, G., & Jones, R. E. (1988). Exsolved silicate and oxide phases from clinopyroxenes in a single Hawaiian xenolith—Implications for oxidation-state of the Hawaiian upper mantle. *Geology*, *16*(1), 69–72. https://doi.org/10.1130/0091-7613(1988)016<0069:ESAOPF>2.3.CO;2
Shive, P. N., Frost, B. R., & Peretti, A. (1988). The magnetic-properties of metaperidotitic rocks as a function of metamorphic grade - implications for crustal magnetic-anomalies. *Journal of Geophysical Research*, *93*(B10), 12,187–12,195. https://doi.org/10.1029/JB093iB10p12187
Siedlecka, A., Roberts, D., Nystuen, J. P., & Olovyanishnikov, V. G. (2004). Northeastern and northwestern margins of Baltica in Neoproterozoic time: Evidence from the Timanian and Caledonian Orogens. *Geological Society, London, Memoirs*, *30*(1), 169–190. https://doi.org/10.1144/GSL.MEM.2004.030.01.15

SkyTEM surveys, 2011, SkyTEM survey: Lokkarfjord and Reinfjord Finnmark County, Norway, Data report: Technical report prepared for Nordic Mining ASA, september 2011

Strada, E., Talarico, F. M., & Florindo, F. (2006). Magnetic petrology of variably retrogressed eclogites and amphibolites: A case study from the Hercynian basement of northern Sardinia (Italy). *Journal of Geophysical Research*, *111*, B12S26. https://doi.org/10.1029/2006JB004574

Tauxe, L. (1998). *Paleomagnetic principles and practice* (Vol. 17). Dordrecht: Springer Science & Business Media. https://doi.org/10.1007/0-306-48128-6

Thébault, E., Finlay, C. C., Beggan, C. D., Alken, P., Aubert, J., Barrois, O., et al. (2015). International Geomagnetic Reference Field: the 12th generation. *Earth Planets and Space*, *67*, 79. https://doi.org/10.1186/s40623-015-0228-9

Thébault, E., Purucker, M. E., Whaler, K. A., Langlais, B., & Sabaka, T. J. (2010). The magnetic field of the Earth's lithosphere. *Space Science Reviews*, *155*(1–4), 95–127. https://doi.org/10.1007/s11214-010-9667-6

Verwey, E. J. W. (1939). Electronic conduction of magnetite (Fe3O4) and its transition point at low temperatures [5]. *Nature*, *144*(3642), 327–328. https://doi.org/10.1038/144327b0

Wang, C. Y., Zhou, M.-F., Yang, S., Qi, L., & Sun, Y. (2014). Geochemistry of the Abulangdang intrusion: Cumulates of high-Ti picritic magmas in the Emeishan large igneous province, SW China. *Chemical Geology*, *378-379*(C), 24–39. https://doi.org/10.1016/j.chemgeo.2014.04.010

Warner, R. D., & Wasilewski, P. (1995). Magnetic petrology of lower crust and upper-mantle xenoliths from Mcmurdo Sound, Antarctica. *Tectonophysics*, *249*(1–2), 69–92. https://doi.org/10.1016/0040-1951(95)00014-E

Wasilewski, P., & Mayhew, M. A. (1982). Crustal xenolith magnetic properties and long wavelength anomaly source requirements. *Geophysical Research Letters*, *9*(4), 329–332. https://doi.org/10.1029/GL009i004p00329

Wasilewski, P., & Mayhew, M. A. (1992). The Moho as a magnetic boundary revisited. *Geophysical Research Letters*, *19*(22), 2259–2262. https://doi.org/10.1029/92GL01997

Wasilewski, P., & Warner, R. D. (1988). Magnetic petrology of deep crustal rocks - Ivrea zone, Italy. *Earth and Planetary Science Letters*, *87*(3), 347–361. https://doi.org/10.1016/0012-821X(88)90022-2

Wasilewski, P. J., Thomas, H. H., & Mayhew, M. A. (1979). The Moho as a magnetic boundary. *Geophysical Research Letters*, *6*(7), 541–544. https://doi.org/10.1029/GL006i007p00541

Williams, M. C., Shive, P. N., Fountain, D. M., & Frost, B. R. (1985). Magnetic-properties of exposed deep crustal rocks from the Superior Province of Manitoba. *Earth and Planetary Science Letters*, *76*(1–2), 176–184. https://doi.org/10.1016/0012-821X(85)90157-8

Yeo, W. J. A. (1984). *The Melkvann Ultramafic Complex, Seiland Igneous Province*. Department of Geology: University of Bristol.

Ziemniak, S. E., & Castelli, R. A. (2003). Immiscibility in the Fe3O4–FeCr2O4 spinel binary. *Journal of Physics and Chemistry of Solids*, *64*(11), 2081–2091. https://doi.org/10.1016/S0022-3697(03)00237-3